Redox Biology 93 (2026) 104176

Contents lists available at ScienceDirect

Redox Biology

journal homepage: www.elsevier.com/locate/redox

Peroxiredoxin III safeguards cardiac function against doxorubicin by regulating mitochondrial quality control via H_2O_2 detoxification

Ji Won Park [a], Se Yeon Jang [a], Mi Yeon Kim [a], Ho Jin Yi [b], Seong Keun Sonn [c], Okhee Kweon [c], Byung-Hoon Lee [a,d], Goo Taeg Oh [c], Hyun Ae Woo [b,e,**], Tong-Shin Chang [a,d,*]

[a] College of Pharmacy and Research, Seoul National University, 1 Gwanak-ro, Gwanak-gu, Seoul, 08826, Republic of Korea
[b] College of Pharmacy, Graduate School of Applied Science and Technology for Skin Health and Aesthetics, Ewha Womans University, Seoul, 120-750, Republic of Korea
[c] Heart-Immune-Brain Network Research Center, Department of Life Science, Ewha Womans University, Seoul, 03760, Republic of Korea
[d] Research Institute of Pharmaceutical Sciences, Seoul National University, 1 Gwanak-ro, Gwanak-gu, Seoul, 08826, Republic of Korea
[e] College of Pharmacy, Graduate School of Pharmaceutical Sciences, Ewha Womans University, Seoul, 120-750, Republic of Korea

ARTICLE INFO

Keywords:
Doxorubicin
Cardiotoxicity
Mitochondrial quality control
Oxidative stress
Peroxiredoxin III

ABSTRACT

Doxorubicin (DOX) is a widely used anticancer drug associated with severe cardiotoxicity primarily driven by mitochondrial dysfunction and reactive oxygen species (ROS) production. Hydrogen peroxide (H_2O_2), a major mitochondrial ROS, significantly contributes to cardiotoxicity, yet its precise mechanistic role in DOX-induced cardiotoxicity remains incompletely understood. Here, we investigated the critical role of mitochondrial H_2O_2 in DOX-induced cardiotoxicity using rat cardiomyocyte H9c2 cells with stable knockdown or reconstitution of mitochondrial antioxidant enzyme peroxiredoxin III (PrxIII), which specifically regulates mitochondrial H_2O_2 levels. Our results demonstrated that severe mitochondrial H_2O_2 accumulation (>10-fold compared to control) in PrxIII-depleted cells exacerbated mitochondrial oxidative stress, evidenced by increased cardiolipin oxidation and mitochondrial membrane potential dissipation. Furthermore, excessive mitochondrial H_2O_2 impaired mitochondrial fusion by reducing fusion-related protein expression, disrupted autophagic flux via lysosomal dysfunction, and significantly attenuated mitophagy, ultimately leading to enhanced apoptosis. Conversely, moderate mitochondrial H_2O_2 levels (5- to 8-fold increase compared to control) observed in PrxIII-expressing cells promoted mitochondrial elongation, enhanced mitophagy, and preserved autophagic flux, suggesting a protective adaptation against DOX-induced oxidative stress. *In vivo* experiments using PrxIII knockout mice confirmed that loss of PrxIII aggravated DOX-induced cardiac dysfunction. Bioinformatic analysis of independent public transcriptome datasets and targeted qPCR validation in PrxIII-deficient cardiac tissues further confirmed that the mitochondrial quality control pathways identified *in vitro* are robustly dysregulated *in vivo*. Additionally, PrxIII deficiency markedly increased mitochondrial structural damage without significantly affecting cardiac fibrosis or hypertrophy. Notably, mitigating the mitochondrial H_2O_2 burden and protecting the mitochondrial inner membrane using the mitochondria-targeted antioxidant peptide SS-31 successfully rescued this exacerbated cardiac dysfunction. In conclusion, our findings establish mitochondrial H_2O_2 as a pivotal determinant in DOX-induced mitochondrial dysfunction and cardiotoxicity, highlighting PrxIII as a promising therapeutic target for mitigating oxidative cardiac injury.

1. Introduction

Doxorubicin (DOX) is a widely used anthracycline anticancer drug that exerts therapeutic effects by inhibiting topoisomerase II, leading to DNA damage, impaired DNA synthesis, and subsequent cell death [1,2]. Specifically, DOX forms complexes with tyrosine residues of topoisomerase II, disrupting gene expression and initiating apoptotic pathways

* Corresponding author. College of Pharmacy and Research Institute of Pharmaceutical Sciences, Seoul National University, 1 Gwanak-ro, Gwanak-gu, Seoul, 08826, Republic of Korea.
** Corresponding author. College of Pharmacy, Graduate School of Pharmaceutical Sciences, Ewha Womans University, Seoul, 120-750, Republic of Korea.
E-mail addresses: jw3611@snu.ac.kr (J.W. Park), hena08@naver.com (S.Y. Jang), nicemy94@naver.com (M.Y. Kim), yihoz@naver.com (H.J. Yi), ssk999@ewha.ac.kr (S.K. Sonn), okirella@ewha.ac.kr (O. Kweon), lee@snu.ac.kr (B.-H. Lee), gootaeg@ewha.ac.kr (G.T. Oh), hawoo@ewha.ac.kr (H.A. Woo), changts@snu.ac.kr (T.-S. Chang).

https://doi.org/10.1016/j.redox.2026.104176
Received 19 November 2025; Received in revised form 15 April 2026; Accepted 16 April 2026
Available online 16 April 2026
2213-2317/© 2026 The Authors. Published by Elsevier B.V. This is an open access article under the CC BY-NC-ND license (http://creativecommons.org/licenses/by-nc-nd/4.0/).

Abbreviations:

•OH	hydroxyl radical
7-AAD	7-aminoactinomycin
10-NAO	10-N-nonylacridine orange
Ad-GFP-LC3	recombinant adenoviral vector encoding GFP-tagged LC3
Ad-GFP-mCherry-LC3	recombinant adenoviral vector encoding tandem fluorescent-tagged LC3
Ad-PrxIII	recombinant adenoviral vector encoding the full-length human PrxIII cDNA
BafA1	bafilomycin A1
BNIP3	Bcl2 adenovirus e1B 19 kDa interacting protein 3
CM-H_2DCFDA	5-(and-6)-chloromethyl-2′,7′-dichlorodihydrofluorescein diacetate
CO	cardiac output
cTnI	cardiac troponin I
DAPI	4′,6-diamidno-2-phenylindole
DOX	doxorubicin
Drp1	dynamin-related protein 1
EF	ejection fraction
FOXO3a	Forkhead box O3a
FS	fractional shortening
FUNDC1	FUN14 domain-containing 1
GAPDH	glyceraldehyde 3-phosphate dehydrogenase
Gpx	glutathione peroxidase
H_2O_2	hydrogen peroxide
HR	heart rate
KO	knockout
LAMP1	lysosome-associated membrane protein 1
LC3	light-chain 3
LVESV	left ventricular end-systolic volume
Mfn	mitofusin
MiNA	mitochondrial network analysis
MitoPY-1	mitochondria peroxy yellow-1
mPTP	mitochondrial permeability transition pore
MQC	mitochondrial quality control
mTOR	mammalian target of rapamycin
mtTFA	mitochondrial transcription factor A
Nrf1	nuclear respiratory factor 1
$O_2•^-$	superoxide radical
OCR	oxygen consumption rate
OPA1	optic atrophy 1
PARP-1	poly(ADP-ribose) polymerase 1
PFA	paraformaldehyde
PGC-1α	peroxisome proliferator-activated receptor gamma coactivator-1 alpha
PINK1	PTEN-induced kinase-1
Prx	peroxiredoxin
qRT-PCR	quantitative real time polymerase chain reaction
Rho-123	Rhodamine-123
ROS	reactive oxygen species
SOD	superoxide dismutase
SV	stroke volume
WST-1	2-(4-iodophenyl)-3-(4-nitrophenyl)-5-(2,4-disulfophenyl)-2H-tetrazolium monosodium salt
WT	wild-type
$\Delta\Psi_m$	mitochondrial membrane potential

[3,4]. DOX has been widely used to treat various cancers and was estimated to have a market share of close to $20 million in 2021 with an increasing compound annual growth rate of 10.7% [5]. Despite its potent anticancer efficacy, the clinical use of DOX is severely limited by its dose-dependent cardiotoxicity, which remains a critical barrier to its broader application [6,7].

A central mechanism underlying DOX-induced cardiotoxicity involves mitochondrial oxidative stress, primarily driven by excessive generation of reactive oxygen species (ROS) within cardiac mitochondria [8,9]. Due to its strong affinity for cardiolipin, a phospholipid abundant in the mitochondrial inner membrane, DOX preferentially accumulates in cardiac mitochondria [10]. This accumulation increases ROS generation through electron leakage from the mitochondrial electron transport chain, particularly at complexes I and III, enhancing the formation of superoxide radicals ($O_2•^-$) [11,12]. Superoxide anions produced in the mitochondrial matrix are rapidly converted to hydrogen peroxide (H_2O_2) by superoxide dismutase (MnSOD or SOD2) [13]. Although H_2O_2 itself is relatively less reactive, it is membrane-permeable and can diffuse throughout cellular compartments, propagating oxidative stress. Furthermore, mitochondrial H_2O_2 can readily convert to highly reactive hydroxyl radicals (•OH) via the Fenton reaction, catalyzed by iron-sulfur clusters and other divalent metal ions abundant in mitochondria [14,15]. Consequently, the precise regulation of mitochondrial H_2O_2 levels is essential for mitigating oxidative stress and associated cardiac damage.

Cells have evolved multiple antioxidant systems to counteract mitochondrial ROS toxicity, among which peroxiredoxin III (PrxIII) plays an especially critical role. PrxIII, a mitochondria-specific antioxidant enzyme, effectively detoxifies H_2O_2 into water with high catalytic efficiency, attributable to its low K_m and rapid turnover rate [16,17]. Indeed, previous studies, including our own, have consistently demonstrated the pivotal role of PrxIII in protecting various cell types against mitochondrial oxidative stress and associated cellular damage under pathological conditions [18–20]. However, the relationship between mitochondrial H_2O_2 levels modulated by PrxIII activity and alterations in mitochondrial dynamics under DOX-induced cardiotoxicity remains inadequately understood.

Mitochondria are dynamic organelles regulated by mitochondrial quality control (MQC) mechanisms, including mitochondrial biogenesis [21], mitochondrial fusion/fission, and mitophagy [22,23]. Mitophagy selectively eliminates damaged mitochondria via autophagosomal degradation [24], whereas mitochondrial biogenesis replenishes the mitochondrial pool by generating new organelles through transcriptional activation [25]. Mitochondria fusion, mediated by mitofusins (Mfn1 and Mfn2) and optic atrophy 1 (OPA1), dilutes mitochondrial damage by merging impaired mitochondria with functional ones. Conversely, fission, orchestrated by dynamin-related protein 1 (Drp1), facilitates removal of irreversibly damaged mitochondrial segments [26]. Disruption of the balance between mitochondrial fusion and fission contributes significantly to mitochondrial dysfunction and cardiac injury following DOX exposure [27–29]. Emerging evidence indicates that mitochondrial H_2O_2 levels critically regulate various MQC processes, suggesting a mechanistic link between oxidative stress and MQC dysregulation.

In this study, we investigated how modulation of mitochondrial H_2O_2 levels through PrxIII alteration affects mitochondrial dynamics and cardiotoxicity following DOX exposure, using *in vitro* and *in vivo* models with differential PrxIII expression. Our findings highlight the crucial protective role of PrxIII in maintaining mitochondrial integrity and suggest that precise control of mitochondrial H_2O_2 could significantly attenuate DOX-induced cardiac damage, offering a potential therapeutic strategy to enhance the clinical safety of DOX treatment.

2. Materials and methods

2.1. Reagents and antibodies

DOX was kindly provided from Donga-ST Co., Ltd. (Seoul, Republic of Korea); Fetal Bovine Serum (FBS) and antibiotic-antimycotic (A/A) were from Gibco (NY, USA); Dimethyl sulfoxide (DMSO), poly-L-lysine, puromycin, and bafilomycin A1 (BafA1) were from Sigma-Aldrich (St. Louis, MO, USA); 2-(4-iodophenyl)-3-(4-nitrophenyl)-5-(2,4-disulfophenyl)-2H-tetrazolium monosodium salt (WST-1) reagent was purchased from Roche Applied Science (Basel, Switzerland); Lipofectamine 2000, 5-(and-6)-chloromethyl-2′,7′-dichlorodihydrofluorescein diacetate (CM-H2DCFDA), Rhodamine-123 (Rho-123), Mitotracker Red CMX, Lysosensor Green DND-189, DQ-BSA and 7-Aminoactinomycin D (7-AAD) were purchased from Invitrogen (CA, USA); 10-N-nonylacridine orange (10-NAO) was purchased from Molecular Probes (Eugene, OR, USA); Mitochondria peroxy yellow-1 (MitoPY-1) was from Tocris Biosciences (Bristol, UK); Magic Red kit was from ImmunoChemistry Technologies (Davis, CA, USA); paraformaldehyde (PFA), 4′,6-diamidno-2-phenylindole (DAPI) were from Thermo Fisher Scientific (Waltham, MA, USA); Adenosine triphosphate (ATP) and cell viability ATP assay kit was from Promega (Madison, WI, USA); Seahorse XF cell Mitostress test kit, Seahorse XF DMEM Medium, and Seahorse XF Calibrant Solution was from Agilent (Santa Clara, CA, USA); Elamipretide (SS-31) was from Biorbyt Ltd. (Cambridge, UK); Mitoquinone (MitoQ) and Visomitin (SKQ1) were from MedChemExpress (Monmouth junction, NJ, USA); Mouse Troponin I ELISA kit was from Abcam (Cambridge, UK).

The primary antibodies against poly(ADP-ribose) polymerase (PARP), cleaved caspase-3, pDrp1 (Ser616), light-chain 3B (LC3B), SQSTM1/p62, thioredoxin 2 (Trx2), lysosome-associated membrane protein 1 (LAMP1), nuclear respiratory factor (Nrf1), forkhead box O3a (FOXO3a) were purchased from Cell Signaling Technology (Danvers, MA, USA); Parkin, Bcl2 adenovirus e1B 19 kDa interacting protein 3 (BNIP3), Drp1, Bax, peroxisome proliferator-activated receptor gamma coactivator 1-alpha (PGC-1α), Mfn1 and Mfn2 were purchased from Santa Cruz Biotechnologies (Dallas, TX, USA); PrxV, OPA1, PTEN-induced kinase 1 (PINK1) and mitochondria transcription factor (mtTFA) were purchased from Abcam (Cambridge, UK); Tomm20 was from Sigma-Aldrich (St. Louis, MO, USA); catalase, glutathione peroxidase IV (GpxIV), superoxide dismutase 2 (SOD2), α-tubulin, β-actin and PrxIII (mono) were purchased from Ab Frontier (Seoul, Republic of Korea); glyceraldehyde 3-phosphate dehydrogenase (GAPDH) was purchased from Chemicon (Jincheon, Republic of Korea); The secondary antibodies against anti-mouse IgG HRP and anti-rabbit IgG HRP were purchased from Seracare (Milford, MA, USA).

2.2. Cell culture

Rat cardiomyocyte cell line, H9c2 cells (CRL-1446) were obtained from the American Type Culture Collection (Manassas, VA, USA) and cultured in DMEM high glucose (SH30022.01, Hyclone, Logan, UT, USA) supplemented with 10% FBS, 1% antibiotic-antimycotic, and 1 μg/ml puromycin. Cells were fed every 2-3 days and maintained at 37 °C with a humidified 5% CO_2 incubator.

To generate a plasmid expressing a short hairpin RNA specific for rat PrxIII, two complementary oligonucleotides targeting the 5′-AAGAGCUGAGUCUCGACGACU-3′ sequence within the open reading frame of rat PrxIII mRNA were synthesized (Genotech, Daejeon, Republic of Korea):

5′-GATCCCCGAGCTGAGTCTCGACGACTTTCAAGAGAAGTCGTCGAGACTCAGCTCTTTTTA-3′

5′-AGCTTAAAAAGAGCTGAGTCTCGACGACTTCTCTTGAAAGTCGTCGAGACTCAGCTCGGG-3′ The oligonucleotides were annealed and ligated into the pSUPER-puro vector (VEC-pBS-0008; OligoEngine, Seattle, WA, USA), resulting in the short hairpin RNA-expressing construct pSUPER-siPrxIII.

H9c2 cells were transfected with either pSUPER-siPrxIII or control pSUPER vectors using Lipofectamine 2000 transfection reagent according to the manufacturer's instructions. After 48 h, cells were selected with puromycin (1 μg/mL), and puromycin-resistant clones were isolated and expanded.

2.3. Adenovirus construction and transfection

To overexpress human PrxIII, a recombinant adenoviral vector encoding the full-length human PrxIII cDNA (Ad-PrxIII) was constructed and packaged by VectorBuilder (vector ID: VB220222-1017kpd, Chicago, IL, USA). An adenoviral vector carrying a non-coding stuffer sequence (Ad-Stuffer, vector ID: VB220301-1013hty, VectorBuilder) was used as a control.

For monitoring autophagy, adenoviral vectors encoding GFP-tagged LC3 (Ad-GFP-LC3) or tandem fluorescent-tagged LC3 (Ad-GFP-mCherry-LC3) were used, as described previously [30].

All adenoviral transductions were performed in serum-free medium for 4 h, followed by replacement with complete medium and incubation for 20 h before analysis.

2.4. Drugs

DOX stock solution was 2 mg/mL and diluted in DMEM to make a final concentration. DOX was treated in DMEM at indicated concentration for indicated times. BafA1 dissolved in DMSO for culture and treated at 10 nM for 4 h.

2.5. Cell viability assay

Cells were seeded in 96-well plates and incubated for 24 h. WST-1 reagent (10 μL) was added to each well, and plates were incubated for 1 h at 37 °C in the dark. Absorbance at 440 nm was measured using a SpectraMax i3x plate reader (Molecular Devices, San Jose, CA, USA).

2.6. Measurement of ROS

To measure intracellular ROS and mitochondrial H_2O_2, cells were cultured in 6-well plates until they reached approximately 80% confluence. After DOX treatment, cells were stained with 5 μM CM-H_2DCFDA or MitoPY-1 [31] for 15 min at 37 °C in the dark. A minimum of 2×10^5 cells per sample was used for each measurement. Cells were analyzed using a FACSLyric flow cytometer (BD bioscience, San Jose, CA, USA), and the relative fluorescence intensity was quantified using FlowJo software 10.9 (FlowJo LLC, Ashland, OR, USA).

To measure mitochondrial H_2O_2 with images, cells were grown for 24 h in 12-well plates with poly-L-lysine-coated cover glass. After DOX treatment, cells were stained with 10 μM MitoPY-1 for 15 min at 37 °C in the dark, washed with PBS, and fixed for 15 min with 4% PFA solution. Confocal images were captured using the TCS8 confocal microscope (Leica, Wetzlar, Germany). Five random fields per sample were selected, and the mean relative fluorescence intensity was calculated using ImageJ software (NIH, Bethesda, MD, USA).

2.7. Immunofluorescence analysis

For visualization of the location of FOXO3a, immunostaining of FOXO3a and localization to nucleus was assessed. Seeded cells were washed with PBS and fixed with 4% paraformaldehyde at 4 °C for 15 min. Then, the cells were permeabilized using 0.1% Triton X-100 at RT for 15 min and washed with PBS before being blocked with 3% (w/v) BSA in PBS for 1 h at RT. Subsequently, cells were incubated with primary antibodies against FOXO3a at a 1:300 dilution overnight at 4 °C. After three washes in the blocking solution, the cells were incubated

with the secondary antibodies, Alexa Fluor 488 goat anti-mouse IgG (H + L) (A-11001, Thermo Fisher Scientific, Waltham, MA, USA) for 2 h at RT and then washed three more times in blocking solution. Finally, the cells were stained with DAPI before being imaged. Fixed cells were examined with the TCS8 confocal microscopy (Leica, Wetzlar, Germany). Images were analyzed using ImageJ/Fiji software.

2.8. Determination of mitochondrial damage

To assess mitochondrial lipid oxidation, cardiolipin oxidation was measured using 10-NAO. After DOX treatment, cells were stained in 5 μM 10-NAO at 37 °C in the dark for 15 min [32]. Mitochondrial membrane potential ($\Delta\Psi_m$) was measured using 10 μM Rho-123 under similar conditions. Stained cells were analyzed using a FACSLyric flow cytometer, and the relative fluorescence intensity was quantified using FlowJo software.

2.9. ATP assay

Intracellular ATP levels were quantified using the CellTiter-Glo 2.0 Assay (Promega, Madison, WI, USA) according to the manufacturer's instructions with modifications for quantification. Briefly, cells were plated in white opaque 96-well plates and treated with DOX. At the endpoint, CellTiter-Glo reagent was added at 1:1 ratio to culture medium, and the mixture was incubated for 10 min at RT to stabilize luminescence signals. Luminescence was measured using a microplate reader. To determine absolute ATP concentrations, a standard curve was generated in parallel using serial dilutions of ATP prepared in assay buffer, and sample ATP levels were calculated by interpolating luminescence values against the standard curve. ATP concentrations were normalized to protein contents determined from replicate wells using the BSA assay.

2.10. Oxygen consumption rate measurement

Oxygen consumption rate (OCR) was measured using Seahorse XFe 96 or XFp analyzer (Agilent Technologies, Santa Clara, CA, USA) accompanied by an Agilent Seahorse Mito Stress test kit (Agilent Technologies) according to the manufacturer instruction. Cells were treated with oligomycin (1 μM), carbonyl cyanide-4-(trifluoromethoxy) phenylhydrazone (FCCP; 1 μM), and a mixture of rotenone/antimycin A (0.5 μM) for the measurement of key parameters of mitochondrial respiration. OCR values were normalized to protein contents determined from replicate wells using the BSA assay.

2.11. Immunoblot analysis

Cells were lysed with a buffer containing 20 mM HEPES (pH 7.0), 150 mM NaCl, 1% TritonX-100, 10% glycerol, 2 mM EGTA, 1 mM EDTA, 20 mM glycerol 2-phosphate, 1 mM Na_3VO_4, 1 μg/ml aprotinin, 1 μg/ml leupeptin, and 1 mM AEBSF. Lysates were centrifuged at 12,500×*g* for 10 min at 4 °C, and protein concentrations were measured by Bradford assay. Equal amounts of protein were separated by SDS-PAGE and transferred to a nitrocellulose membrane (Whatman, Maidstone, UK). Membranes were blocked with 5% BSA for 1 h at RT, incubated overnight with primary antibodies at 4 °C, and probed with HRP-conjugated secondary antibodies in 5% skim milk for 1 h at RT. Protein bands were visualized using WESTSAVE-up ECL substrate (Ab frontier, Seoul, Republic of Korea) and detected using an Amersham Imager 680 (GE Healthcare, Chicago, IL, USA). Band density was quantified with ImageJ/Fiji software (NIH, Bethesda, MD, USA).

2.12. Quantitative real time polymerase chain reaction (qRT-PCR) analysis

RNA was prepared from cells using Easy-Blue Total RNA extraction Kit (iNtRON, Seoul, Republic of Korea) and cDNA was synthesized using QuantiTect Reverse Transcription Kit (Qiagen, Hilden, Germany). The resulting cDNA was amplified by qRT-PCR using iTaq Universal SYBR Green Supermix (Bio-Rad, Hercules, CA, USA). The sequences of primers used for qRT-PCR are listed in TableS1.

2.13. Mitochondrial fragmentation measurement

Cells were seeded on poly-L-lysine-coated coverslips in 6-well plates and cultured for 24 h. After treatment, cells were stained with 30 nM MitoTracker Red for 15 min at 37 °C in the dark, then fixed with 4% PFA for 15 min. Confocal images were taken with the TCS8 confocal microscope, and mitochondrial morphology was quantified using aspect ratio analysis with the Mitochondrial Network Analysis (MiNA) plugin Fiji software [33]. Expression levels of mitochondrial fission and fusion proteins (Drp1, Drp1-phospho-Ser616, Mfn1, Mfn2, and OPA1) were determined by immunoblotting.

2.14. Autophagic flux analysis

Autophagic flux was evaluated by Western blotting for LC3B and SQSTM1/p62, and additionally using fluorescence-based LC3 reporters (GFP-LC3 and mCherry-GFP-LC3) as previously described [34]. Cells were transduced with GFP-LC3 adenovirus or GFP-mCherry-LC3 adenovirus for 4 h. It was then changed to full media and incubated for 20 h. After treatment, cells were fixed with 4% PFA solution for 15 min. The images were taken with the TCS8 confocal microscopy, and puncta were measured using Image J Fiji software.

2.15. Lysosomal blockage analysis

Immunofluorescence analysis was performed as described previously [30]. For measurement of lysosomal acidity or activity, cells were loaded with Lysosensor Green DND-189 or Magic Red reagent in a prewarmed media for 1 h after treatment. Then the cells were washed 3 times with PBS and fixed with 4% PFA solution for 15 min. Either, cells were preloaded with 10 μg/ml DQ-BSA Red in prewarmed media for 12 h. They were washed with PBS and fixed with 4% PFA. Additionally, to visualize the lysosome and autophagosome co-localization, fixed cell samples transfected with GFP-LC3 virus were exposed to a blocking solution and incubated at RT for 30 min with antibodies to LAMP1. The cells were washed 3 times with PBS and then incubated with Alexa Fluor 546-conjugated secondary antibodies for 30 min at RT. All images were captured with the TCS8 confocal microscope. Fluorescence was quantified using Image J/Fiji software.

2.16. Apoptosis assay

Detached cells were stained with Annexin V-FITC (25 mM) and 7-AAD (1 μg/ml) in HEPES-glucose and incubated on ice in the dark for 30 min. Fluorescence was analyzed with a FACSLyric flow cytometer, and apoptotic cells were quantified using FlowJo software. In addition, cleaved PARP-1 and cleaved caspase-3 were assessed by Western blotting as described above.

2.17. Animals and in vivo treatment protocols

PrxIII Wild-type (WT) and knockout (KO) mice were generated by breeding heterozygous mice. 8- to 10-week-old male C57BL/6J mice (Jackson Laboratory, Bar Harbor, ME, USA) were used for all experiments. Animal care and experimental procedures were conducted in compliance with the guidelines approved by the Institutional Animal Care and Use Committee of Ewha Womans University and Seoul National university (EWHA IACUC 21-034-t, SNU IACUC 251224-5). Animals were housed in temperature-controlled conditions (20–22 °C) with a 12-h light/dark cycle.

For the evaluation of acute DOX-induced cardiotoxicity, PrxIII WT and KO mice were treated with DOX (10 mg/kg, intraperitoneally) for 2 weeks. After administration, cardiac function was assessed using echocardiography, and histological samples were collected to evaluate cardiac mitochondrial damage and fibrosis.

To comprehensively evaluate the comparative efficacy of mitochondria-targeted antioxidants and to conduct the definitive rescue study, a 4-week chronic DOX cardiotoxicity model was established. Mice were administered DOX (5 mg/kg once weekly via intraperitoneally (i.p.) injection for 4 weeks) to induce chronic cardiac dysfunction. In the comparative pilot study, WT mice were randomly assigned to receive saline, DOX alone, or DOX combined with daily i.p. injections of the following mitochondria-targeted antioxidants: MitoQ (5 mg/kg), SKQ1 (0.3 mg/kg), or SS-31 (3 mg/kg). Body weights were regularly monitored throughout the experimental period to assess systemic toxicity.

Based on the superior safety and efficacy profile observed in the pilot study, SS-31 was selected for the definitive rescue experiment. WT and PrxIII KO mice were subjected to the 4-week chronic DOX regimen with or without daily concurrent administration of SS-31 (3 mg/kg, i.p.). At the experimental endpoint, cardiac function was thoroughly evaluated using echocardiography, and blood samples were collected to measure serum cardiac Troponin I (cTnI) levels for the assessment of structural cardiomyocyte injury.

2.18. Transthoracic echocardiography

Cardiac function was assessed by transthoracic echocardiography using the Vevo 2100 system (FUJIFILM Visual Sonics Inc., Toronto, ON, Canada) equipped with a 25–55-MHz linear array transducer at Ewha Fluorescence Core Imaging Center. Mice (10 weeks old) were anesthetized with 1.5–2% isoflurane, and the mice body temperature was maintained at 37 °C using a homeothermic heating pad throughout the imaging. Heart rate (HR) was continuously monitored and maintained above 450 bpm to ensure physiological conditions. Left ventricular (LV) parameters, including the ejection fraction (EF), fractional shortening (FS), stroke volume (SV), cardiac output (CO), LV end-systolic volume (LVESV), and HR were evaluated in the parasternal long-axis view using Simpson's monoplane method of disks with Vevo Strain software (FUJIFILM Visual Sonics Inc.).

2.19. Damaged mitochondria analysis using transmission electron microscopy (TEM)

For TEM analysis of mitochondrial ultrastructure, heart tissues were harvested from 10-week-old PrxIII WT and KO mice. Sample preparation and TEM analysis were adapted and modified from previously described protocols [35]. Damaged mitochondria were visualized using a transmission electron microscope (JEM-1011, JEOL, Japan) operated at an acceleration voltage of 80 kV. The structural integrity and presence of mitochondrial damage, such as disrupted cristae structure and abnormal morphology, were qualitatively assessed and documented.

2.20. Cardiac fibrosis analysis

To evaluate cardiac fibrosis, left ventricular (LV) tissues from paraffin-embedded heart samples were sectioned at a thickness of 6 μm and stained with Masson's trichrome stain using a commercially available kit (BBC Biochemical, Mount Vernon, WA, USA), following the manufacturer's instructions. Whole-slide images of the stained sections were obtained using the automated quantitative pathology imaging system (Vectra Polaris, PerkinElmer, Waltham, MA, USA). Quantitative analysis of the fibrotic area relative to total LV tissue area (%) was performed using the inForm Advanced Imaging Analysis Software (PerkinElmer).

2.21. Serum cardiac troponin I (cTnI) analysis

Serum cardiac troponin I levels were measured using a mouse cTnI ELISA kit (Abcam, Cambridge, UK), according to the manufacturer's instructions. Blood samples were collected from mice at the endpoint of the experiment and allowed to clot at RT. Serum was obtained by centrifugation at 1500×*g* for 10 min at 4 °C. Standards and samples were added to antibody-coated wells and incubated with the HRP-conjugated detection antibody. After washing, substrate solution was added, and absorbance was measured at 450 nm using a microplate reader. Serum cTnI concentrations were calculated from a standard curve generated with known cTnI standards.

2.22. Bioinformatic analysis of public transcriptome datasets

To independently validate the signaling pathways examined in our study at the transcriptomic level, we analyzed publicly available gene expression datasets from the NCBI Gene Expression Omnibus (GEO) database. We selected datasets from DOX-induced cardiotoxicity models in mice based on the following criteria: (1) cardiac tissue or cardiomyocyte origin, (2) DOX-treated versus vehicle control comparison, and (3) availability of raw count data or processed expression matrices.

Three datasets meeting these criteria were included in the analysis: GSE233644 (mouse heart, DOX 20 mg/kg single i.p. vs sham, n = 4/group, RNA-seq), GSE236165 (mouse heart, DOX 20 mg/kg single i.p. vs PBS, n = 2/group, RNA-seq), and GSE224157 (mouse heart, DOX 5 mg/kg weekly × 4 weeks vs vehicle, n = 3/group, RNA-seq). Processed count or FPKM data were downloaded directly from GEO.

For RNA-seq count data (GSE233644, GSE224157), raw read counts were normalized to counts per million (CPM) and $\log_2$-transformed after adding a pseudocount of 1. Genes with mean expression below 10 counts across all samples were excluded as low-expression filters. For FPKM-based data (GSE236165), $\log_2(\text{FPKM} + 1)$ values were used directly. Differential expression analysis was performed using unpaired two-tailed Student's t-test, and p-values were adjusted for multiple testing using the Benjamini–Hochberg false discovery rate (FDR) correction. Genes with adjusted $p < 0.05$ were considered statistically significant.

A curated panel of 27 target genes was assembled representing seven functional categories central to our study: mitochondrial antioxidant defense (Prdx3, Prdx5, Sod2, Cat, Gpx4, Txn2), mitochondrial biogenesis (Ppargc1a, Nrf1, Tfam), mitochondrial fusion (Mfn1, Mfn2, Opa1), mitochondrial fission (Dnm1l, Fis1), mitophagy/autophagy (Pink1, Prkn, Bnip3, Map1lc3b, Sqstm1, Lamp1), transcription factor (Foxo3), and apoptosis (Casp3, Parp1, Bbc3, Phlda3, Bax, Bcl2). The expression changes of these target genes were visualized as volcano plots and heatmaps, and cross-dataset consistency was evaluated by comparing $\log_2$ fold-change values across independent datasets. All analyses were performed using Python 3.10 with pandas (v1.5), SciPy (v1.10), matplotlib (v3.7), and seaborn (v0.12) libraries.

2.23. Quantitative real-time PCR (qPCR) analysis of cardiac tissues

Total RNA was extracted from frozen cardiac tissues using TRIzol Reagent according to the manufacturer's protocol. Tissues were homogenized using an electric tissue homogenizer on ice. RNA concentration and purity were assessed by NanoDrop spectrophotometry ($A260/A280 \geq 1.8$). cDNA was synthesized using QuantiTect Reverse Transcription Kit (Qiagen, Hilden, Germany). The resulting cDNA was amplified by qRT-PCR using iTaq Universal SYBR Green Supermix (Bio-Rad, Hercules, CA, USA). The sequences of primers used for qRT-PCR are listed in TableS1.

2.24. Western blot analysis of cardiac tissues

Frozen cardiac tissues were lysed in ice-cold 1 × RIPA buffer supplemented with protease inhibitors and phosphatase inhibitors. Tissues

were homogenized using a bead homogenizer and incubated for 30 min at 4 °C. Lysates were centrifuged at 15,000 rpm for 10 min at 4 °C, and the supernatant was collected. Protein concentration was determined by the Bradford assay (Bio-Rad) using BSA as a standard. Equal amounts of protein were separated by SDS-PAGE and transferred to a nitrocellulose membrane (Whatman, Maidstone, UK). Membranes were blocked with 5% BSA for 1 h at RT, incubated overnight with primary antibodies at 4 °C, and probed with HRP-conjugated secondary antibodies in 5% skim milk for 1 h at RT. Protein bands were visualized using WESTSAVE-up ECL substrate (Ab frontier, Seoul, Republic of Korea) and detected using an Amersham Imager 680 (GE Healthcare, Chicago, IL, USA). Band density was quantified with ImageJ/Fiji software (NIH, Bethesda, MD, USA).

2.25. Statistics

Data analysis was performed using GraphPad PRISM software (San Diego, CA, USA). All data are presented as the mean ± standard deviation (S.D.). Statistical significance between multiple groups was primarily analyzed using two-way analysis of variance (ANOVA), followed by Bonferroni's post hoc test. For comparison of multiple experimental groups against a control group, statistical significance was determined using one-way ANOVA, followed by Dunnett's post hoc test. For experiments requiring comparisons between two groups only, statistical analysis was performed using Student's t-test (two-tailed). Statistical significance was considered at a threshold of $p < 0.05$.

3. Results

3.1. DOX increases mitochondrial H_2O_2 and mitochondrial oxidative damage in rat cardiomyocytes

According to previous studies, DOX induces cell damage due to radicals and ROS generated during the redox process of the mitochondrial electron transport chain [36]. We first assessed the toxicity of DOX in H9c2 rat cardiomyocyte cells. At 24 h after DOX treatment, cell death was significantly increased in a concentration-dependent manner (Fig. 1A). Based on this, the DOX concentration was fixed at 1 μM for all subsequent experiments. Treatment with 1 μM DOX significantly reduced the viability of H9c2 cells in a time-dependent manner (Fig. 1B). Intracellular ROS levels were significantly increased 12 h after DOX treatment as assessed using the oxidant-sensitive fluorescent probe CM-H_2DCFDA (Fig. 1C). Although CM-H_2DCFDA is commonly used to measure cellular ROS, this probe lacks specificity for individual oxidants and the ability to distinguish between mitochondrial ROS and other cellular ROS [37]. Therefore, mitochondrial-specific H_2O_2 production was specifically assessed using MitoPY-1. Mitochondrial H_2O_2 levels were significantly elevated after 12 h of DOX exposure (Fig. 1D). Based on these observations, the selected time points and conditions were used in subsequent experiments throughout this study.

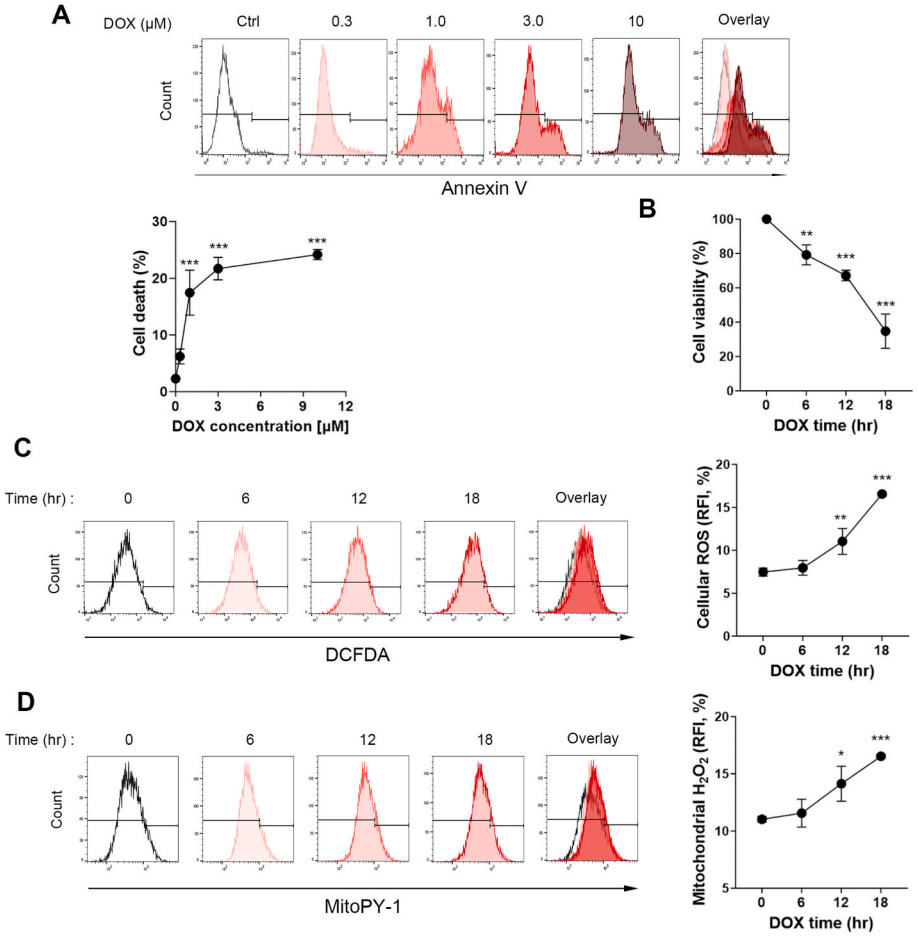


Fig. 1. Doxorubicin increases mitochondrial H_2O_2 levels and causes cell death in rat cardiomyocytes.
(A) H9c2 cells were treated with the indicated concentrations of DOX for 24 h. Cell death was assessed by Annexin V-FITC staining and analyzed using flow cytometer. Representative histograms of three independent experiments are shown. (B) H9c2 cells were treated with 1 μM DOX for the indicated times. Cell viability was measured using WST-1 reagent. (C-D) H9c2 cells were treated with 1 μM DOX for the indicated times and then stained with 5 μM CM-H_2DCFDA (C) or 5 μM MitoPY-1 (D) for 15 min. Relative fluorescence intensity (RFI) was measured by flow cytometer. All data are presented as mean ± S.D. (n = 3). Statistical significance was determined by one-way ANOVA followed by Dunnett's post hoc test. *$p < 0.05$, **$p < 0.01$, ***$p < 0.001$ compared to untreated control.

3.2. Excessive mitochondrial H_2O_2 exacerbates DOX-induced mitochondrial oxidative damage

PrxIII is a mitochondrion-localized peroxidase that serves as the major enzymatic defense against H_2O_2 within the mitochondrial matrix. Unlike other antioxidant enzymes such as catalase, glutathione peroxidase (Gpx), or SOD2, PrxIII directly detoxifies H_2O_2 generated by mitochondrial metabolism, thereby maintaining intramitochondrial redox balance [16,38]. Given its dominant role in H_2O_2 removal, we sought to investigate how modulation of PrxIII expression—and the resulting differences in mitochondrial H_2O_2 levels—affects the susceptibility of cardiomyocytes to DOX-induced injury. To this end, we established stable PrxIII knockdown rat cardiomyocytes (Fig. S1A) and reconstituted ectopic PrxIII in the PrxIII knockdown cells to precisely modulate mitochondrial H_2O_2 levels (Fig. S1C).

Importantly, to determine whether the depletion of PrxIII induces compensatory alterations in other cellular antioxidant defense systems, which could confound our observations, we evaluated the basal expression levels of major antioxidant enzymes in pSUPER and pSUPER-siPrxIII cells. As shown in Supplementary Fig. S1B, the expression levels of other key hydrogen peroxide-scavenging enzymes (catalase, GpxIV, and PrxV), the mitochondrial superoxide-scavenging enzyme (SOD2), and the mitochondrial thioredoxin (Trx2) remained unchanged despite the robust knockdown of PrxIII. These results indicate that the baseline antioxidant network is not globally altered by PrxIII depletion. Therefore, the observed exacerbation of DOX-induced oxidative damage in PrxIII-depleted cells is specifically attributable to the loss of PrxIII function, highlighting its indispensable and non-redundant role in mitochondrial H_2O_2 detoxification.

Mitochondrial H_2O_2 accumulation induced by DOX was first assessed using the mitochondrial-specific fluorescent probe MitoPY-1. After 9 h of DOX treatment, mitochondrial H_2O_2 levels were significantly increased in pSUPER-siPrxIII cells compared to control (pSUPER) cells, whereas ectopic PrxIII reconstitution restored mitochondrial H_2O_2 levels to baseline (Fig. 2A). Quantitative analysis defined two distinct oxidative stress conditions in our experimental system: moderate oxidative stress, characterized by an approximately 5- to 8-fold increase in mitochondrial H_2O_2 levels compared to control, and excessive oxidative stress, defined as >10-fold increase.

To examine how mitochondrial H_2O_2 levels determine redox signaling, we analyzed FOXO3a localization as a functional readout of redox threshold sensing. FOXO3a, a redox-sensitive transcription factor that mediates antioxidant defense and mitochondrial adaptation [39,40]. In response to DOX, FOXO3a exhibited robust nuclear accumulation in control cells but markedly failed to enter the nucleus in pSUPER-siPrxIII cells with excessive H_2O_2 accumulation (Fig. 2B). These findings indicate that the difference between moderate and excessive mitochondrial H_2O_2 is not merely quantitative but represents distinct biological states.

3.3. Excessive mitochondrial H_2O_2 exacerbates DOX-induced oxidative damage and impairs mitochondrial function

Accumulated mitochondrial H_2O_2 can promote oxidative damage of mitochondrial macromolecules, such as cardiolipin, leading to mitochondrial membrane rupture and subsequent dissipation of $\Delta\Psi_m$ [41,42]. Cardiolipin, a mitochondria-specific phospholipid critically involved in oxidative phosphorylation and apoptosis regulation [43,44], was markedly oxidized in pSUPER-siPrxIII cells relative to control after 12 h of DOX treatment. However, PrxIII reconstruction significantly reduced cardiolipin oxidation (Fig. 3A). Consistently, $\Delta\Psi_m$ dissipation, assessed using the cationic dye Rho-123 [45], was significantly enhanced in pSUPER-siPrxIII cells compared to control cells, indicating mitochondria membrane destabilization under excessive oxidative stress (Fig. 3B).

To assess whether excessive mitochondrial H_2O_2 due to PrxIII

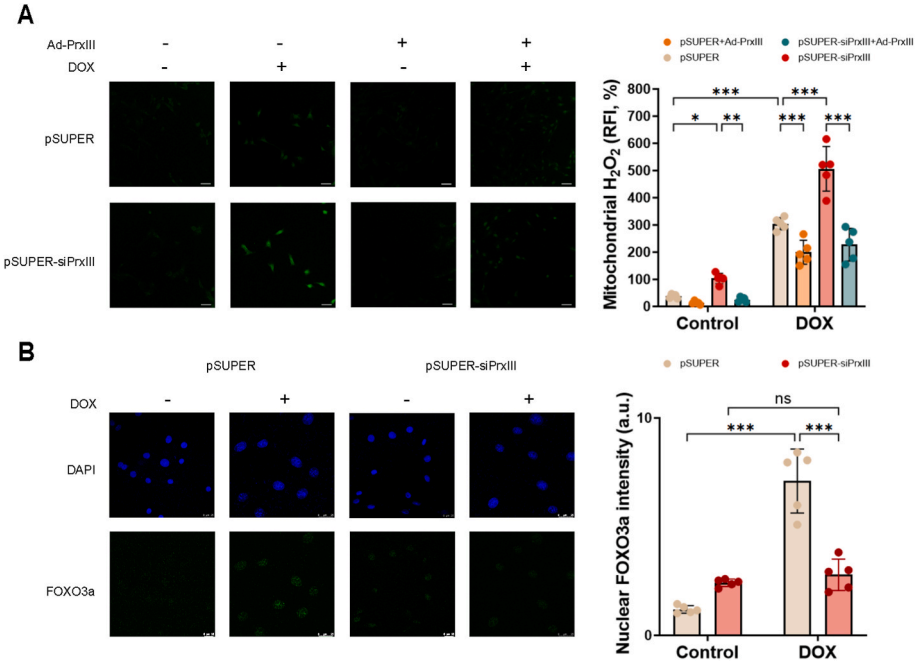


Fig. 2. PrxIII regulates mitochondrial H_2O_2 accumulation and oxidative damage in DOX-treated cardiomyocytes.
(A) H9c2 cells stably expressing either control (pSUPER) or PrxIII-targeting siRNA (pSUPER-siPrxIII) were transduced with Ad-PrxIII or Ad-Stuffer for 24 h and then exposed to 1 μM DOX for 9 h. Mitochondrial H_2O_2 levels were assessed using the mitochondria-targeted fluorescent probe MitoPY-1 and visualized by green fluorescence. Scale bar, 75 μm. Five randomly selected microscopic fields per sample were analyzed and combined to represent one biological replicate. (B) Cells were transduced with Ad-PrxIII or Ad-Stuffer for 24 h and then exposed to 1 μM DOX for 18 h. FOXO3a localization was assessed by immunofluorescence using anti-FOXO3a (green) antibody and DAPI (blue). Scale bar, 25 μm Five randomly selected microscopic fields per sample were analyzed and combined to represent one biological replicate. All data are expressed as mean ± S.D. Statistical significance was determined using two-way ANOVA followed by Bonferroni's post hoc test. *$p < 0.05$, **$p < 0.01$, ***$p < 0.001$ and ns, $p > 0.05$.

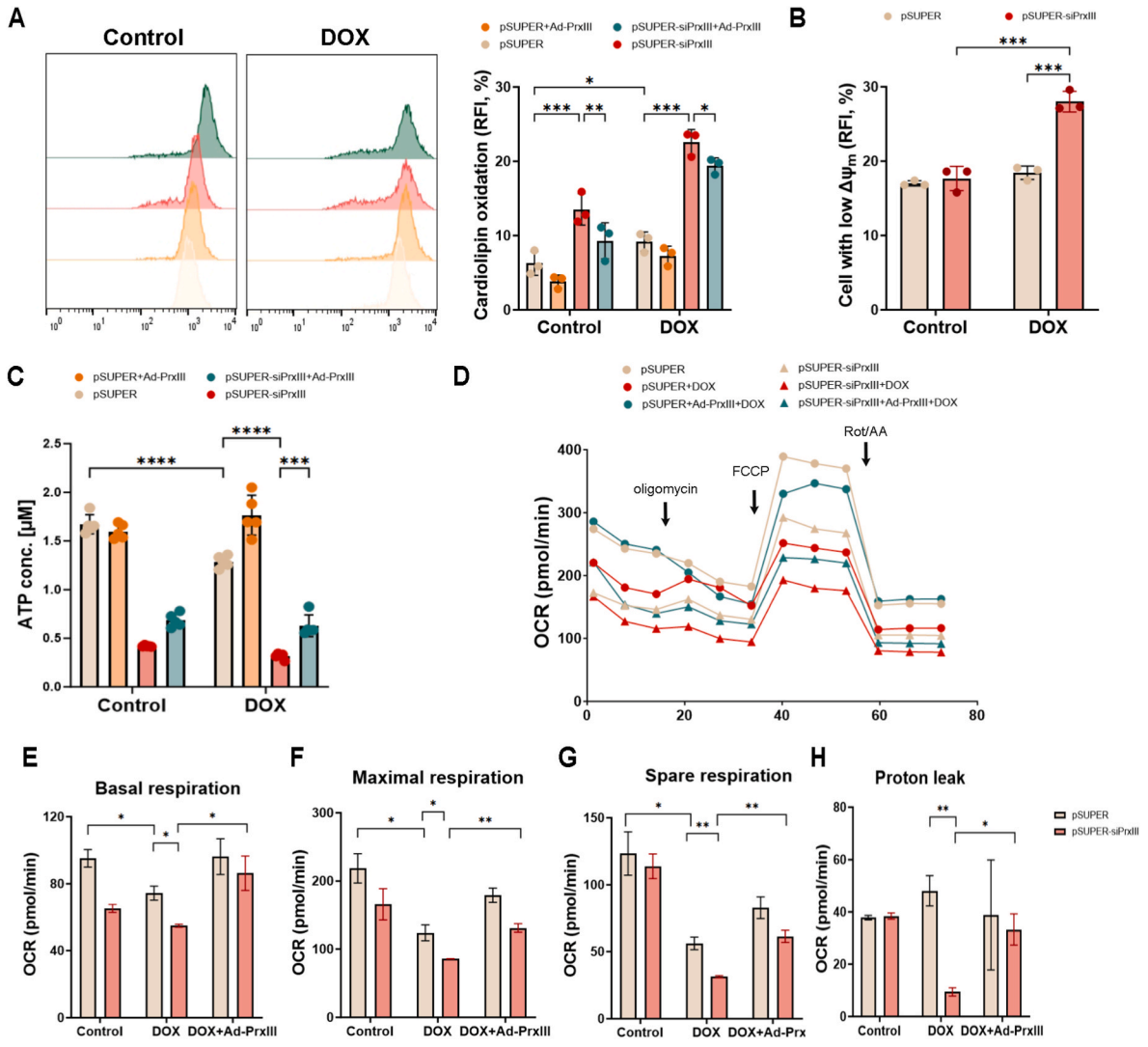


Fig. 3. PrxIII regulates oxidative damage and mitochondrial bioenergetics in DOX-treated cardiomyocytes.
(A) Cells were transduced with Ad-PrxIII or Ad-Stuffer for 24 h and then exposed to 1 μM DOX for 12 h. Cells were labeled with 5 μM 10-NAO and relative fluorescence intensity (RFI) was analyzed by flow cytometer. Representative histograms and quantification are shown. (B) Cells were treated with 1 μM DOX for 12 h and labeled with 10 μM Rho-123 to assess mitochondrial membrane potential ($\Delta\Psi_m$). The percentage of cells with low $\Delta\Psi_m$ was quantified by flow cytometry. Representative histograms and quantification are shown. (C) Cells were transduced with Ad-PrxIII or Ad-Stuffer for 24 h and then exposed to 1 μM DOX for 12 h. Representative bar graph showing relative ATP concentration normalized to protein contents. (D-H) Cells were transduced with Ad-PrxIII or Ad-Stuffer for 24 h and then exposed to 1 μM DOX for 12 h. (D) Representative tracing of the oxygen consumption rate (OCR). Arrows indicate time points when cells were treated with oligomycin, FCCP, and rotenone plus antimycin A (Rot/AA), respectively. The OCR is calculated as (E) basal respiration, (F) maximal respiration, (G) spare respiration, and (H) proton-leak. All data are expressed as mean ± S.D. (n = 3-5). Statistical significance was determined using two-way ANOVA followed by Bonferroni's post hoc test. *$p < 0.05$, **$p < 0.01$, ***$p < 0.001$, and ****$p < 0.0001$.

depletion affects mitochondrial function, we measured parameters reflecting mitochondrial integrity and bioenergetics. Intracellular ATP quantification revealed a strong reduction in pSUPER-siPrxIII cells, even under basal conditions, and a further decrease following DOX exposure, whereas PrxIII re-expression restored ATP levels to near control values (Fig. 3C). We further investigated mitochondrial dysfunction following DOX treatment using extracellular flow analysis to quantify mitochondrial activity by observing the OCR. Bioenergetic analysis with oligomycin, FCCP, and rotenone/antimycin A revealed altered cellular metabolic process [46]. Seahorse analysis demonstrated that DOX treatment significantly reduced basal respiration, maximal respiration, and spare respiratory capacity in pSUPER-siPrxIII cells, while PrxIII re-expression reversed these defects (Fig. 3D–H).

Together, these data indicate that excessive mitochondrial H_2O_2 induces mitochondrial oxidative damage and impairs mitochondrial oxidative phosphorylation, thereby reducing energy generation, while PrxIII maintains basal and stress-induced mitochondrial bioenergetic function.

3.4. *Excessive mitochondrial H_2O_2 suppresses DOX-induced mitochondrial biogenesis*

To determine whether mitochondrial H_2O_2 affects mitochondrial biogenesis, we examined multiple canonical markers of mitochondrial after DOX exposure. Mitochondrial biogenesis is a highly coordinated process that integrates nuclear and mitochondrial transcriptional programs to replenish the mitochondrial population and sustain oxidative capacity [47]. This pathway is primarily governed by the transcriptional co-activator PGC-1α, which serves as a master regulator linking metabolic and redox cues to mitochondrial gene expression [48,49]. PGC-1α co-activates the nuclear transcription factor Nrf1, which in turn induces expression of mitochondrial transcription factor A (mtTFA/TFAM)

[50]—a key protein required for mitochondrial DNA replication, packaging, and transcription [21]. Together, the PGC-1α–Nrf1–TFAM axis drives the synthesis of new mitochondrial components and maintains the balance between mitochondrial degradation and renewal, ensuring proper MQC under physiological and stress conditions.

In control cells, DOX exposure modestly elevated PGC-1α, whereas its downstream transcription factors Nrf1 and mtTFA were reduced. This pattern suggests a limited, compensatory activation of PGC-1α that fails to propagate through the downstream biogenic cascade. In contrast, pSUPER-siPrxIII cells exhibited a marked reduction in PGC-1α expression at both mRNA and protein levels, accompanied by a further decline in Nrf1, and TFAM. These changes reflect global suppression of the nuclear-mitochondrial transcriptional program governing organelle renewal. Re-expression of PrxIII almost completely restored all biogenesis markers to near-control levels (Fig. 4A–C).

mtTFA is essential for packaging and transcribing mitochondrial DNA (mtDNA); its depletion results in impaired mtDNA replication and reduced mitochondrial gene expression [51]. The reduction of mtTFA therefore represents a terminal point of biogenesis failure, translating transcriptional repression into defective organelle replication. To further substantiate the impact on mitochondrial genome expression, we measured the mRNA level of the mtDNA-encoded gene cytochrome *c* oxidase (COX) as an indicator of mitochondrial transcriptional output (Fig. 4B). COX transcripts were markedly decreased in pSUPER-siPrxIII cells following DOX treatment, consistent with reduced mtTFA expression and mtDNA transcriptional activity.

Collectively, these findings demonstrate that PrxIII deficiency leads to coordinated suppression of the entire mitochondrial biogenesis program, encompassing PGC-1α, Nrf1, mtTFA, and mtDNA-encoded genes. The rescue of these parameters by PrxIII re-expression indicates that

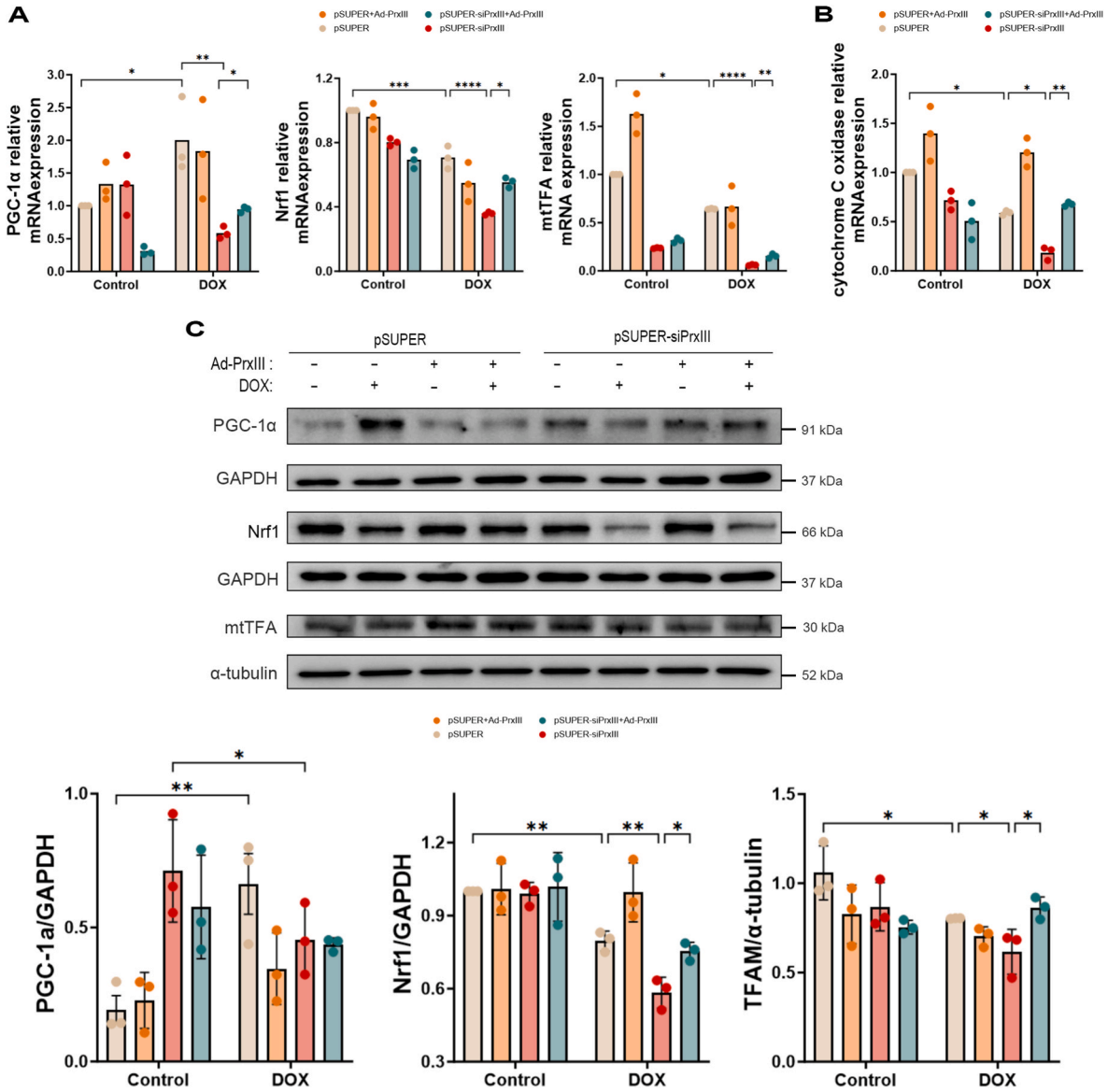


Fig. 4. PrxIII regulates mitochondrial biogenesis in DOX-treated cardiomyocytes.
(A) Cells were transduced with Ad-PrxIII or Ad-Stuffer for 24 h and then exposed to 1 μM DOX for 6 h. Total RNA was isolated and the mRNA levels of PGC-1α, Nrf1, and mtTFA were determined by qRT-PCR. Representative bar graphs showing relative expression normalized to GAPDH are presented. (B) Relative mRNA expression of the mitochondrial DNA-encoded cytochrome *c* oxidase (COX) mRNA was measured as an indicator of mtDNA copy-dependent transcription. Representative bar graphs showing relative expression normalized to GAPDH are presented. (C) Cells were transduced with Ad-PrxIII or Ad-Stuffer for 24 h and then exposed to 1 μM DOX for 18 h. Representative immunoblots and quantitative analyses of PGC-1α, Nrf1, and mtTFA proteins. GAPDH and α-tubulin were used as loading controls. Densitometric quantification of protein expression was performed from three independent biological replicates. All data are presented as mean ± S.D. (n = 3). Statistical significance was determined using two-way ANOVA followed by Bonferroni's post hoc test. *p < 0.05, **p < 0.01, ***p < 0.001, and ****p < 0.0001.

mitochondrial H_2O_2 homeostasis is critical not only for degradation pathways such as mitophagy but also for the transcriptional renewal of mitochondria. Thus, PrxIII functions as a pivotal regulator that maintains balanced mitochondrial turnover by coupling redox buffering with biogenic signaling under oxidative stress conditions.

3.5. Excessive mitochondrial H_2O_2 suppresses DOX-induced mitochondrial elongation and induces imbalance of the MQC system

Mitochondria dynamics are maintained through a delicate balance between mitochondrial fission and fusion. Alterations in mitochondrial morphology reflect disruptions in this balance. Disruption of mitochondrial dynamics can lead to mitochondrial dysfunction and subsequent cellular damage [26,27]. To determine how DOX treatment and mitochondrial H_2O_2 levels influence mitochondrial dynamics, we compared mitochondrial morphology and expression of mitochondrial fusion and fission markers in pSUPER and pSUPER-siPrxIII cells. After 12 h of DOX exposure, mitochondria were notably elongated in pSUPER cells; however, they did not significantly change in pSUPER-siPrxIII cells. Importantly, reconstitution of PrxIII in pSUPER-siPrxIII cells restored mitochondrial elongation after DOX treatment (Fig. 5A). These results suggested that a moderate level of mitochondrial H_2O_2 promotes mitochondrial elongation, potentially serving as a protective mechanism against oxidative stress, whereas excessive H_2O_2 accumulation impaired this adaptive response.

We next evaluated the expression levels of protein markers involved in mitochondrial fusion and fission (Fig. 5B). Regarding fusion-related proteins, PrxIII depletion alone increased levels of Mfn1, Mfn2, and OPA1 even in the absence of DOX treatment. Upon DOX exposure, the levels of fusion proteins Mfn1, Mfn2, and OPA1 were increased in control pSUPER cells. In contrast, fusion-related protein levels were significantly decreased in pSUPER-siPrxIII cells compared to control following DOX treatment. Reconstitution of PrxIII rescued the expression of all fusion proteins after DOX exposure.

To investigate mitochondrial fission, we measured the phosphorylation status of Drp1 at serine 616, a post-translational modification known to promote mitochondrial fission [52]. Interestingly, Drp1 phosphorylation levels were not significantly different between pSUPER and pSUPER-siPrxIII after DOX treatment. These results indicate that moderate mitochondrial H_2O_2 levels triggered mitochondrial elongation and fusion, potentially as an adaptive mechanism to mitigate oxidative stress. In contrast, excessive mitochondrial H_2O_2 accumulation, as observed in DOX-treated PrxIII-depleted cells, significantly impaired mitochondrial dynamics, contributing to mitochondrial dysfunction.

3.6. Excessive mitochondrial H_2O_2 impairs autophagic flux and mitophagy

Next, we investigated changes in autophagy induced by DOX in H9c2 cells. During autophagy progression, LC3-I is converted to LC3-II, which directly binds to ubiquitin adapters such as SQSTM1/p62 (hereafter p62) to form autophagosomes, and p62 is subsequently degraded when autophagosomes fuse with lysosome [34,53,54]. Following DOX treatment, LC3-II levels were significantly elevated in control cells but remained unchanged in pSUPER-siPrxIII cells (Fig. 6A). Conversely, p62 protein levels decreased in control cells, whereas accumulation occurred

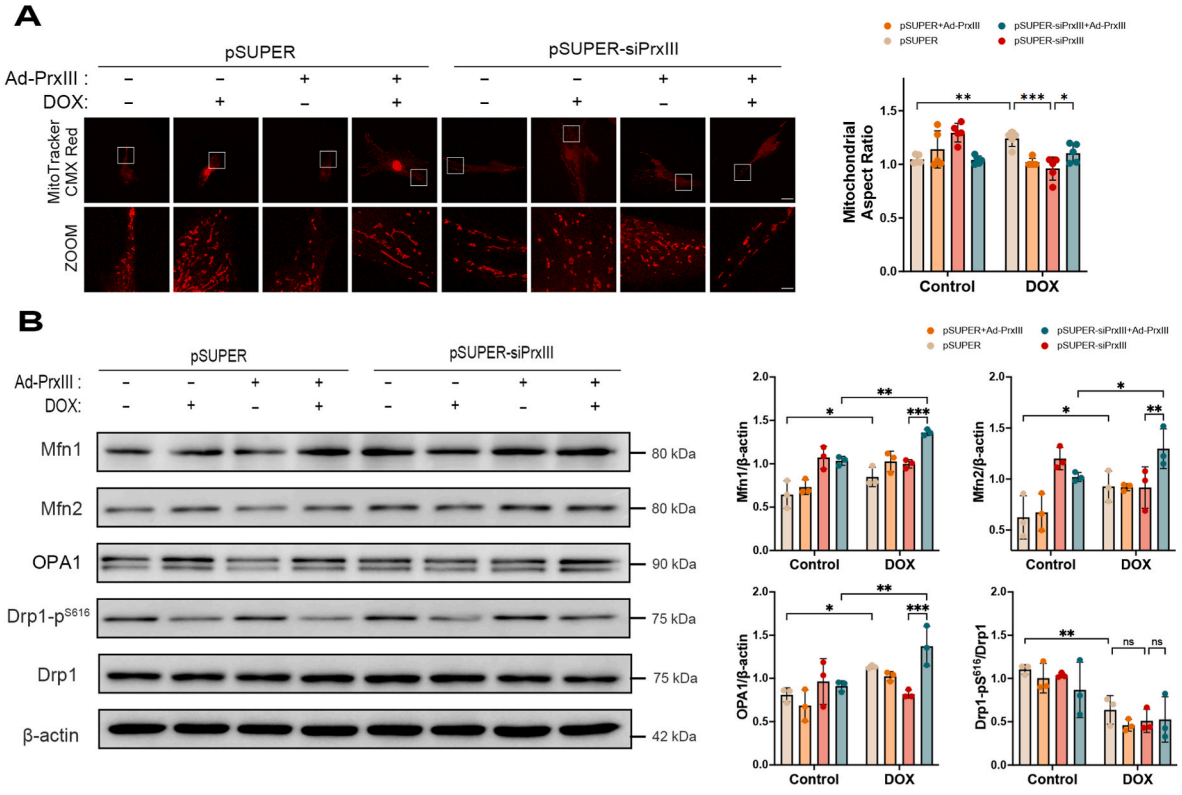


Fig. 5. PrxIII modulates mitochondrial dynamics and prevents mitochondrial imbalance under DOX-induced stress.
(A) Cells were transduced with Ad-PrxIII or Ad-Stuffer for 24 h and then exposed to 1 μM DOX for 12 h. Mitochondria were stained with MitoTracker CMX Red and imaged using confocal microscopy. Mitochondrial morphology was quantified using MiNA plugin Fiji software and expressed as mitochondrial aspect ratio. Enlarged images (labeled "ZOOM") represent magnified views of the boxed regions. Scale bars: 2.5 μm (upper), 0.4 μm (lower). Five randomly selected microscopic fields per sample were analyzed and combined to represent one biological replicate. (B) Cells were treated as described in (A). Western blotting was performed to assess the expression of mitochondrial fusion (Mfn1, Mfn2, and OPA1) and fission (Drp1, Drp1-phospho-Ser616) proteins. β-actin was used as a loading control. Phospho-Drp1 was normalized to total Drp1. Densitometric quantification was performed from three independent biological replicates. All data are presented as mean ± S.D. Statistical significance was determined using two-way ANOVA followed by Bonferroni's post hoc test. *$p < 0.05$, **$p < 0.01$, ***$p < 0.001$, and ns, $p > 0.05$.

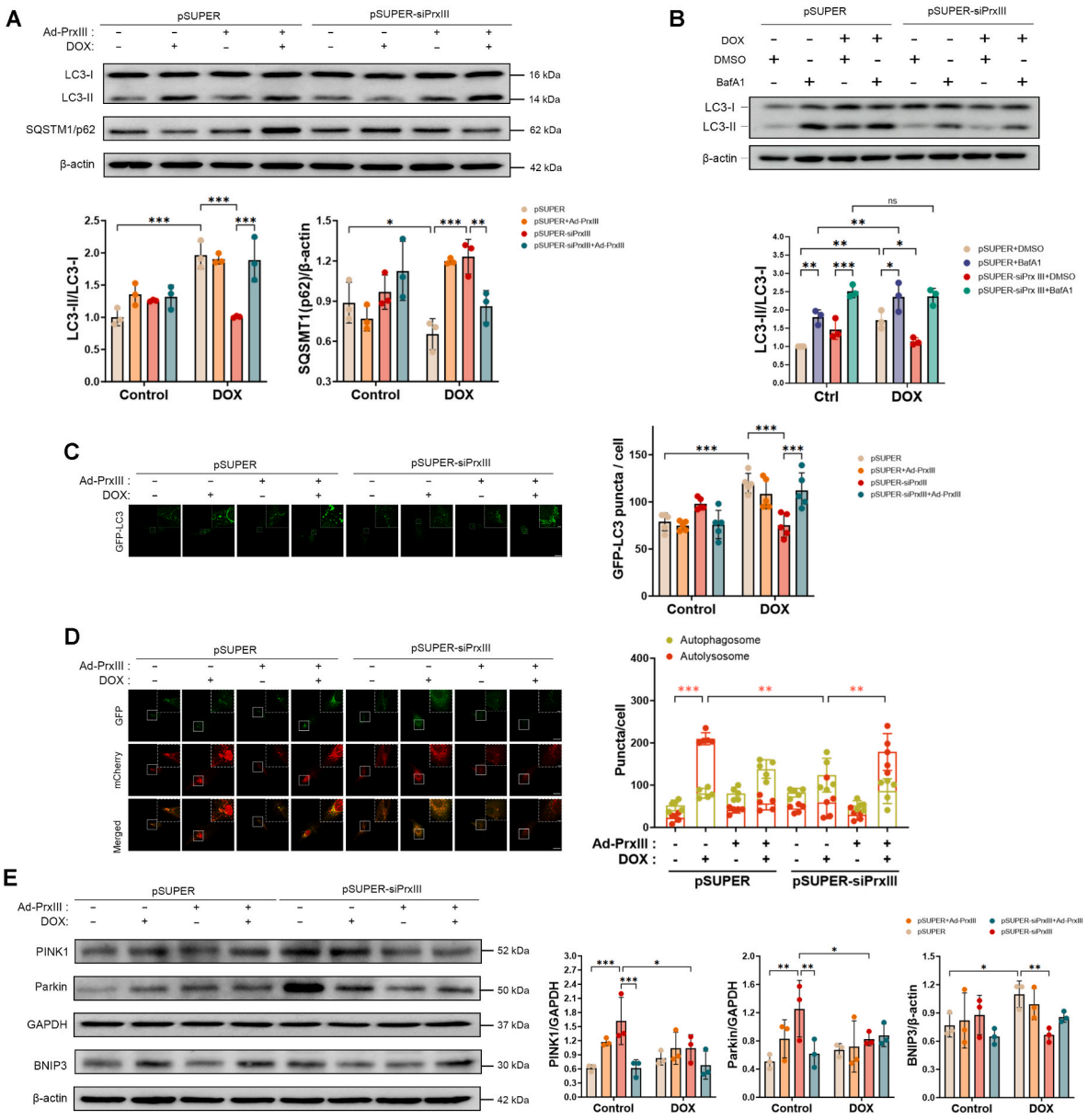


Fig. 6. PrxIII restores impaired autophagic flux and mitophagy under DOX-induced stress.
(A) Cells were transduced with Ad-PrxIII or Ad-Stuffer for 24 h and then exposed to DOX (1 μM, 12 h). Immunoblotting was performed to assess LC3 conversion (LC3-I to LC3-II) and SQSTM1/p62 expression. B-actin was used as a loading control. Densitometric quantification of protein expression was performed from three independent biological replicates. (B) Cells were treated with DOX (1 μM, 6 h) and additionally treated with DMSO or BafA1 (10 nM) for 4 h. Cell lysates were subjected to immunoblot analysis regarding LC3B. β-actin was used as a loading control. Densitometric quantification of protein expression was performed from three independent biological replicates (C-D) Cells were transfected with Ad-PrxIII or Ad-Stuffer in the presence of GFP-LC3 (C) or mCherry-GFP-LC3 (D) adenovirus for 24 h and then exposed to DOX (1 μM, 12 h). Representative confocal images are shown. The upper right image (scale bars, 5 μm) is a magnified image of the white box in each corresponding image (scale bars, 20 μm). Quantitative data of GFP-LC3 puncta (C) or autophagosomes (yellow puncta) and autolysosomes (red puncta) (D) per cell image J/Fiji software. Five randomly selected microscopic fields per sample were analyzed and combined to represent one biological replicate. (E) Immunoblot analysis of PINK1, Parkin, and BNIP3 expression after treatment as described in (B). GAPDH and β-actin were used as loading controls, respectively. Densitometric quantification was performed from three independent biological replicates. All data are presented as mean ± S.D. Statistical significance was determined using two-way ANOVA followed by Bonferroni's post hoc test. *$p < 0.05$, **$p < 0.01$, ***$p < 0.001$, and ns, $p > 0.05$.

in pSUPER-siPrxIII cells after DOX exposure, indicating impaired autophagic flux (Fig. 6A). Importantly, ectopic PrxIII expression in pSUPER-siPrxIII cells restored LC3-II conversion and decreased p62 to levels comparable to control cells.

To further validate autophagic flux, we used BafA1, a lysosomal inhibitor that blocks autophagosome-lysosome fusion and thus causes LC3-II accumulation when autophagy is active [55]. BafA1 alone markedly increased LC3-II accumulation in both control and pSUPER-siPrxIII cells, confirming basal autophagic activity. When combined with DOX, LC3-II levels further increased in control cells compared with BafA1 alone, indicating that DOX-induced autophagy was functionally active. In contrast, pSUPER-siPrxIII cells showed minimal LC3-II induction upon DOX exposure and LC3-II levels in the DOX + BafA1 group were similar to those of BafA1 alone, suggesting impaired autophagosome formation and reduced autophagic flux (Fig. 6B).

We also assessed autophagic flux using image-based methods. First, GFP-LC3 puncta were quantified to confirm autophagosome formation. After 12 h of DOX treatment, GFP-LC3 puncta significantly increased in

control cells but not in pSUPER-siPrxIII cells, indicating defective autophagosome formation under conditions of excessive mitochondrial H_2O_2. Importantly, reconstitution of PrxIII expression in pSUPER-siPrxIII cells restored GFP-LC3 puncta following DOX treatment, reaching levels similar to control cells (Fig. 6C). After autophagosome formation, lysosomes must fuse with autophagosomes to form autolysosomes, facilitating degradation of autophagosomal contents to reduce cellular damage [56,57]. To further analyze autophagic flux, we employed tandem fluorescent-tagged LC3 (mCherry-GFP-LC3) adenovirus, which emits distinct fluorescence signals depending on pH conditions. GFP fluorescence is sensitive to acidic conditions and thus lost in autolysosomes, whereas mCherry fluorescence remains stable. Thus, autophagosomes display combined green and red signals (yellow), whereas autolysosomes exclusively emit red signals [34]. After 12 h of DOX treatment, autophagic flux significantly increased in pSUPER cells but remained impaired in pSUPER-siPrxIII cells. Importantly, re-expression of PrxIII in pSUPER-siPrxIII cells restored autophagy to control levels (Fig. 6D).

In succession, we investigated mitophagy, a specialized autophagy process selectively eliminating damaged mitochondria. We specifically evaluated the PINK1-Parkin-mediated mitophagy and BNIP3-mediated mitophagy pathway [56,58]. After 12 h of DOX treatment, protein levels of PINK1 and BNIP3 increased in control cells but were markedly reduced in pSUPER-siPrxIII cells (Fig. 6E). Interestingly, PINK1 and Parkin expression were significantly elevated in PrxIII-depleted cells even without DOX exposure. These results suggested that excessive mitochondrial H_2O_2 levels induced by DOX in the absence of PrxIII impair the initiation of mitophagy, leaving damaged mitochondria uncleared. Reconstitution of PrxIII in pSUPER-siPrxIII cells effectively restored the levels of PINK1, Parkin, and BNIP3 proteins, indicating successful rescue of mitophagy.

Taken together, these findings demonstrated that moderate

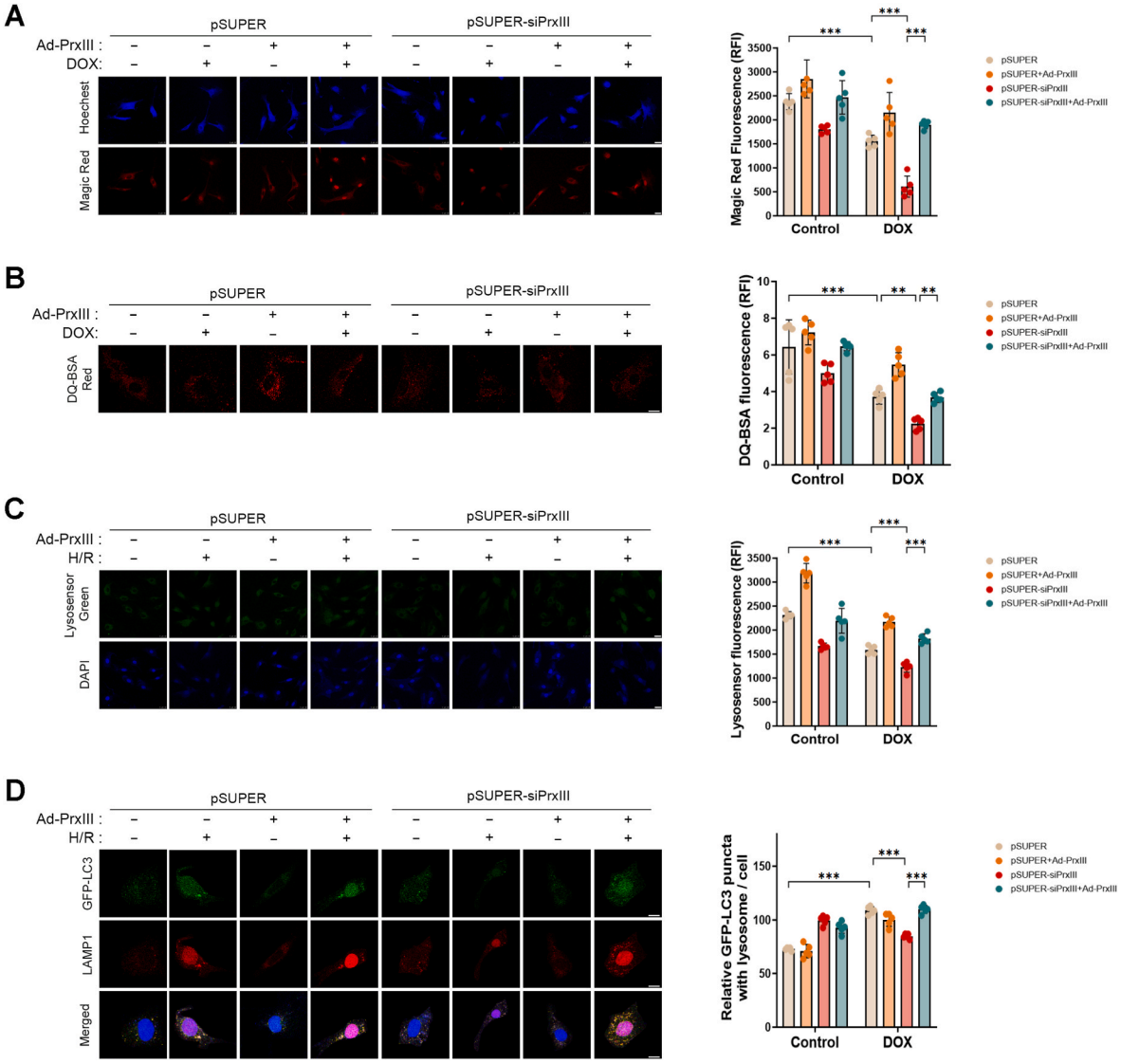


Fig. 7. PrxIII rescues lysosomal dysfunction and promotes autophagosome–lysosome fusion under DOX-induced stress.
Cells were transduced with Ad-PrxIII or Ad-Stuffer for 24 h and then exposed to 1 μM DOX for 6 h. (A) Lysosomal protease activity was analyzed using Magic Red (red), and nuclei were counterstained with Hoechst (blue). Scale bar, 25 μm. (B, C) Lysosomal acidity was analyzed by (B) DQ-BSA Red (red; scale bar, 10 μm) and (C) LysoSensor Green DND-189 (green; scale bar, 25 μm). Nuclei were stained with DAPI (blue). (D) Cells were transduced with Ad-PrxIII or Ad-Stuffer in the presence of GFP-LC3 (green) adenovirus for 24 h and treated as above. Fixed cells were immunostained with anti-LAMP1 antibody (red), and nuclei were stained with DAPI (blue). Colocalization of GFP-LC3 and LAMP1 was plotted as yellow dots in graph. Scale bar, 15 μm. Five randomly selected microscopic fields per sample were analyzed and combined to represent one biological replicate. All data are presented as mean ± S.D. Statistical significance was determined using two-way ANOVA followed by Bonferroni's post hoc test. $^{**}p < 0.01$ and $^{***}p < 0.001$.

mitochondrial H_2O_2 levels induce mitophagy and autophagy as adaptive mechanisms to protect cardiomyocytes from oxidative stress, whereas excessive mitochondrial H_2O_2 accumulation impairs autophagic flux and mitophagy, resulting in accumulation of damaged mitochondria.

3.7. PrxIII depletion inhibits lysosomal activity and fusion with autophagosomes

Autophagic flux can be impaired when lysosomal hydrolase activity is reduced due to elevated lysosomal pH, resulting in impaired fusion of autophagosomes with lysosomes [59,60]. ROS have been shown to affect lysosomal function and contribute to lysosomal blockage [61,62]. To directly assess lysosomal activity, we utilized Cathepsin Magic Red, a substrate that becomes fluorescent upon cleavage by active cathepsins. Fluorescence intensity was significantly decreased in DOX-treated pSUPER-siPrxIII cells, indicating reduced cathepsin B enzymatic activity. Importantly, lysosome activity was restored to control levels upon reconstitution of PrxIII expression (Fig. 7A).

Next, lysosomal pH was assessed using DQ-BSA Red, a self-quenched fluorescent probe that becomes fluorescent upon proteolytic cleavage in the acidic environment of lysosomes [63], and LysoSensor Green, a pH-sensitive dye whose fluorescence intensity increases in acidic lysosomes [64]. DOX treatment strongly reduced fluorescence intensities of both DQ-BSA Red and LysoSensor Green, with a significantly greater reduction observed in pSUPER-siPrxIII cells compared to control cells. These results indicated an elevated lysosomal pH and impaired lysosomal activity upon PrxIII depletion following DOX treatment (Fig. 7B–C). PrxIII reconstitution successfully restored lysosome acidity to levels comparable with pSUPER cells.

To further examine if impaired lysosomal fusion contributed to defective autophagic flux, we transfected cells with GFP-LC3 adenovirus and analyzed colocalization of GFP-LC3 with LAMP1, a marker of

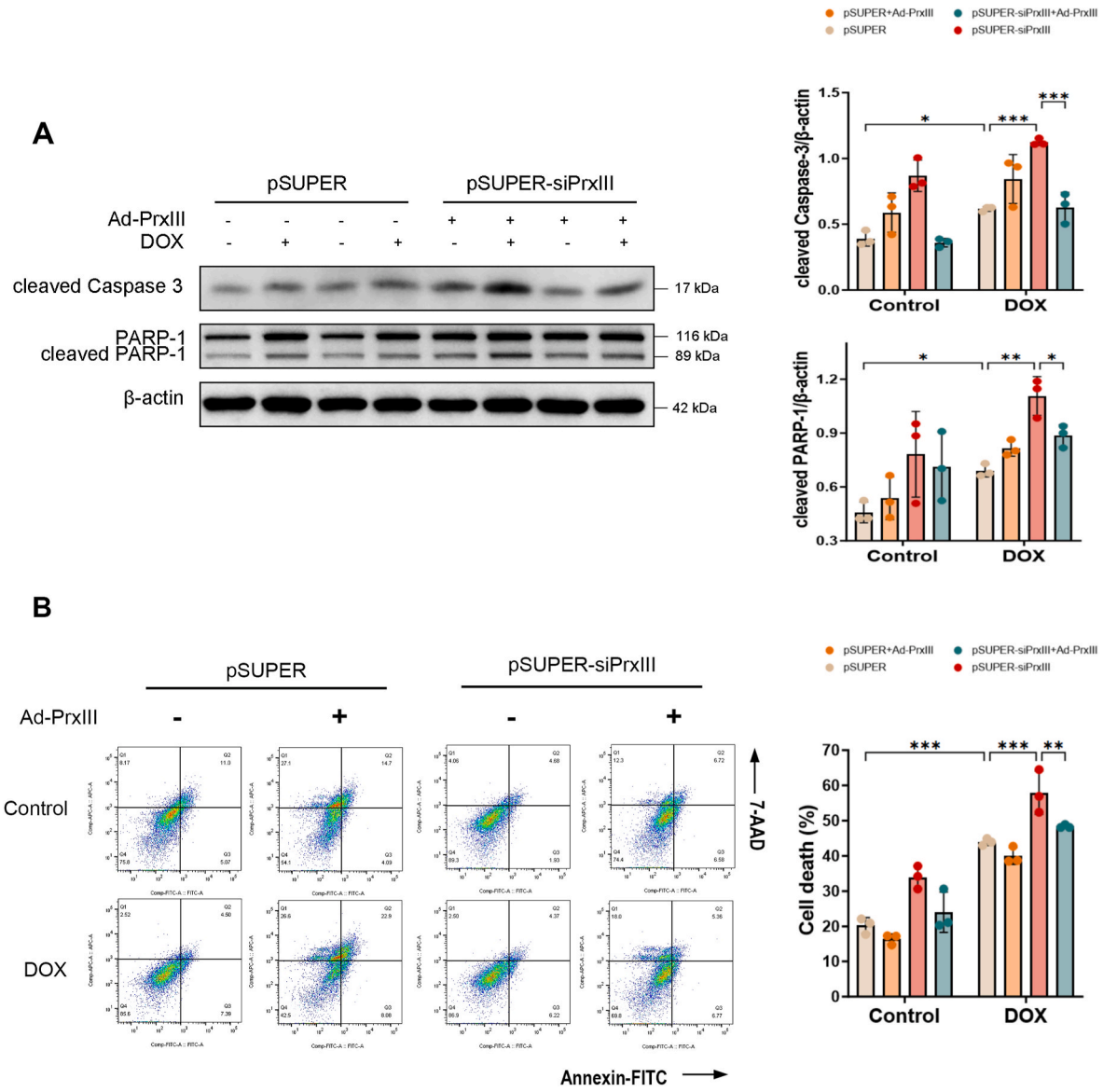


Fig. 8. PrxIII protects cardiomyocytes against DOX-induced apoptotic cell death.
Cells were transduced with Ad-PrxIII or Ad-Stuffer for 24 h and then exposed to 1 μM DOX for 18 h. (A) Cell lysates were subjected to immunoblot analyses for cleaved Caspase-3 and cleaved PARP-1 with normalization to β-actin. Densitometric quantification of protein expression was performed from three independent biological replicates. (B) Apoptotic cell death was assessed by Annexin V-FITC and 7-AAD double staining followed by flow cytometric analysis. Quantification of Annexin V and/or 7-AAD-positive cells is shown. All data are presented as mean ± S.D. Statistical significance was determined using two-way ANOVA followed by Bonferroni's post hoc test. *$p < 0.05$, **$p < 0.01$ and ***$p < 0.001$.

lysosomes and late endosomes [65]. In control cells, GFP-LC3 puncta showed distinct colocalization with LAMP1-positive lysosomes after DOX treatment, indicative of successful autophagosome-lysosome fusion. In contrast, GFP-LC3 and LAMP1 colocalization was significantly decreased in DOX-treated pSUPER-siPrxIII cells, strongly suggesting a failure in autophagosome-lysosome fusion (Fig. 7D).

Collectively, these findings demonstrated that lysosome acidity and activity were severely impaired under conditions of excessive mitochondrial H_2O_2, inhibiting autophagosome-lysosome fusion and consequently blocking autophagic flux. While lysosomal function was moderately impaired at lower mitochondrial H_2O_2 levels, it was still sufficient to support autophagosome-lysosome fusion and maintain autophagic flux.

3.8. Excessive mitochondrial H_2O_2 leads to apoptotic cell death

Oxidative stress and impaired autophagic flux can lead to mitochondrial dysfunction, ultimately triggering apoptotic cell death [66,67]. Finally, we evaluated mitochondria-mediated apoptotic cell death induced by DOX treatment. PARP-1 and caspase 3 are cleaved and activated during mitochondria-mediated apoptosis, and these cleavage events can be readily measured by immunoblot analysis [68,69]. After 18 h of DOX exposure, pSUPER-siPrxIII cells exhibited significantly higher levels of cleaved PARP-1 and cleaved caspase 3 compared to control cells. Notably, re-expression of PrxIII in pSUPER-siPrxIII cells restored cleaved PARP-1 and caspase 3 levels to those observed in control cells (Fig. 8A).

We further directly measured apoptosis by flow cytometric analysis of cells co-stained with Annexin V-FITC and 7-AAD [70]. Consistent with the immunoblot results, apoptotic cell death was significantly increased in pSUPER-siPrxIII cells compared to control cells following 18 h of DOX treatment. Reconstitution of PrxIII expression effectively reduced apoptosis in pSUPER-siPrxIII cells (Fig. 8B). These results demonstrated that DOX-induced cytotoxicity was markedly exacerbated by PrxIII depletion but effectively mitigated by re-expression of PrxIII.

In summary, under normal conditions, PrxIII maintains mitochondrial H_2O_2 at moderate levels, enabling mitochondrial dynamics and mitophagy to proceed effectively, thus preserving cellular homeostasis. Mildly increased mitochondrial H_2O_2 levels induced by either PrxIII knockdown alone or DOX treatments in cells expressing normal PrxIII levels activate mitochondrial fusion and mitophagy to alleviate oxidative stress. However, excessive accumulation of mitochondrial H_2O_2, as observed in PrxIII-depleted cells upon DOX exposure, significantly disrupts mitochondrial dynamics and blocks autophagic flux. Consequently, extensive mitochondrial damage and apoptosis ensue. Our findings strongly suggest that PrxIII serves as a critical protective factor against DOX-induced cardiotoxicity by tightly regulating mitochondrial H_2O_2 levels.

3.9. PrxIII deficiency aggravates cardiac dysfunction after DOX treatment

To evaluate the impact of mitochondrial PrxIII deficiency on cardiac function under DOX-induced stress *in vivo*, we performed longitudinal echocardiographic assessments in WT and PrxIII KO mice before and after DOX treatment (10 mg/kg, intraperitoneally, 2 weeks). Importantly, baseline (pre-DOX) echocardiographic measurements were obtained for all animals immediately prior to DOX administration, enabling within-subject paired comparisons that rigorously distinguish the effects of DOX treatment from potential pre-existing genotype differences. At baseline, both PrxIII WT and KO mice exhibited comparable cardiac function across almost all echocardiographic parameters, including EF, FS, HR, CO, and LVESV, confirming that PrxIII deficiency alone does not impair basal cardiac function. This observation is consistent with previous findings demonstrating normal cardiac function and mitochondrial ultrastructure in PrxIII KO mice under unstressed conditions [35]. Following DOX treatment, PrxIII KO mice exhibited a significantly greater decline in cardiac function compared with WT controls. Notably, while EF, FS, CO, HR, and LVESV were comparable between WT and KO mice at baseline, these parameters deteriorated significantly only after DOX challenge in KO mice, with EF and FS markedly reduced, HR and CO decreased, and LVESV increased compared with WT controls, indicating that PrxIII deficiency specifically exacerbates DOX-induced systolic dysfunction and impaired ventricular emptying. In contrast, SV was already reduced in PrxIII KO mice at baseline, consistent with a previous report [35], and showed no further significant decline after DOX treatment, suggesting that baseline hemodynamic differences in SV are attributable to PrxIII deficiency per se rather than DOX-induced injury. These results underscore that the core pathological impact of PrxIII deficiency under DOX stress is the exacerbation of systolic dysfunction (EF, FS, CO, LVESV), reinforcing the essential role of PrxIII-mediated mitochondrial H_2O_2 detoxification in preserving cardiac contractile function under DOX-induced oxidative stress (Fig. 9A).

Despite the marked functional impairment, heart weight/body weight ratios were comparable between the two groups post-DOX, indicating that the observed cardiac dysfunction occurred independently of hypertrophic remodeling (Fig. 9B). TEM analysis revealed a substantial increase in the numeric density of structurally damaged mitochondria in PrxIII KO hearts compared with WT controls, demonstrating exacerbated mitochondrial injury in the absence of PrxIII (Fig. 9C). Additionally, no significant difference in LV fibrosis was observed between genotypes (Fig. 9D), suggesting that the functional impairment was predominantly attributable to mitochondrial damage rather than fibrotic remodeling. Serum cTnI levels, a sensitive biomarker of cardiomyocyte injury [71,72], were significantly elevated in PrxIII KO mice compared with WT controls following DOX treatment, further confirming enhanced myocardial damage at the biochemical level (Fig. 9E).

Collectively, these *in vivo* findings, employing a longitudinal paired echocardiographic design, robustly demonstrate that PrxIII deficiency critically exacerbates DOX-induced cardiac dysfunction through impaired mitochondrial integrity, reinforcing PrxIII as a pivotal protective factor against DOX-induced cardiotoxicity.

3.10. Public transcriptome analysis of independent GEO datasets confirms DOX-induced dysregulation of MQC pathways

To independently verify that the signaling pathways examined in our *in vitro* study are indeed dysregulated during DOX-induced cardiotoxicity *in vivo*, we performed a systematic bioinformatic analysis of publicly available transcriptomic datasets from the NCBI Gene Expression Omnibus (GEO). We curated 27 target genes representing seven functional categories central to our study: mitochondrial antioxidant defense (including Prdx3, Prdx5, Sod2, Cat, Gpx4, Txn2), mitochondrial biogenesis (Ppargc1a, Nrf1, Tfam), mitochondrial fusion (Opa1, Mfn1, Mfn2), fission (Dnm1l, Fis1), mitophagy/autophagy (Pink1, Prkn, Bnip3, Map1lc3b, Sqstm1, Lamp1), transcription factor (Foxo3), and apoptosis (Casp3, Bax, Parp1,Bcl2, Phlda3, Bbc3) (Fig. 10A–C).

Among the datasets analyzed, GSE233644 (mouse heart, DOX vs sham, n = 4/group) provided the most comprehensive coverage, with 17 of 27 target genes showing statistically significant differential expression (adjusted $p < 0.05$). Notably, mitophagy-related genes were prominently upregulated, including Bnip3 ($+2.82$ $\log_2$FC, $p < 0.01$), Sqstm1/p62 ($+2.72$, $p < 0.01$), Map1lc3b/LC3B ($+1.46$, $p < 0.05$), Pink1 ($+0.76$, $p < 0.05$), and Prkn/Parkin ($+0.56$, $p < 0.01$), whereas mitochondrial fusion gene Opa1 was significantly downregulated (-0.69, $p < 0.01$) along with biogenesis factor Tfam (-0.57, $p < 0.05$) and antioxidant enzyme Sod2 (-0.86, $p < 0.05$). Pro-apoptotic gene Bax was significantly increased ($+0.88$, $p < 0.05$). Cross-dataset comparison with two additional independent heart datasets (GSE236165, GSE224157) confirmed the consistent directionality of these changes, reinforcing the robustness of the findings.

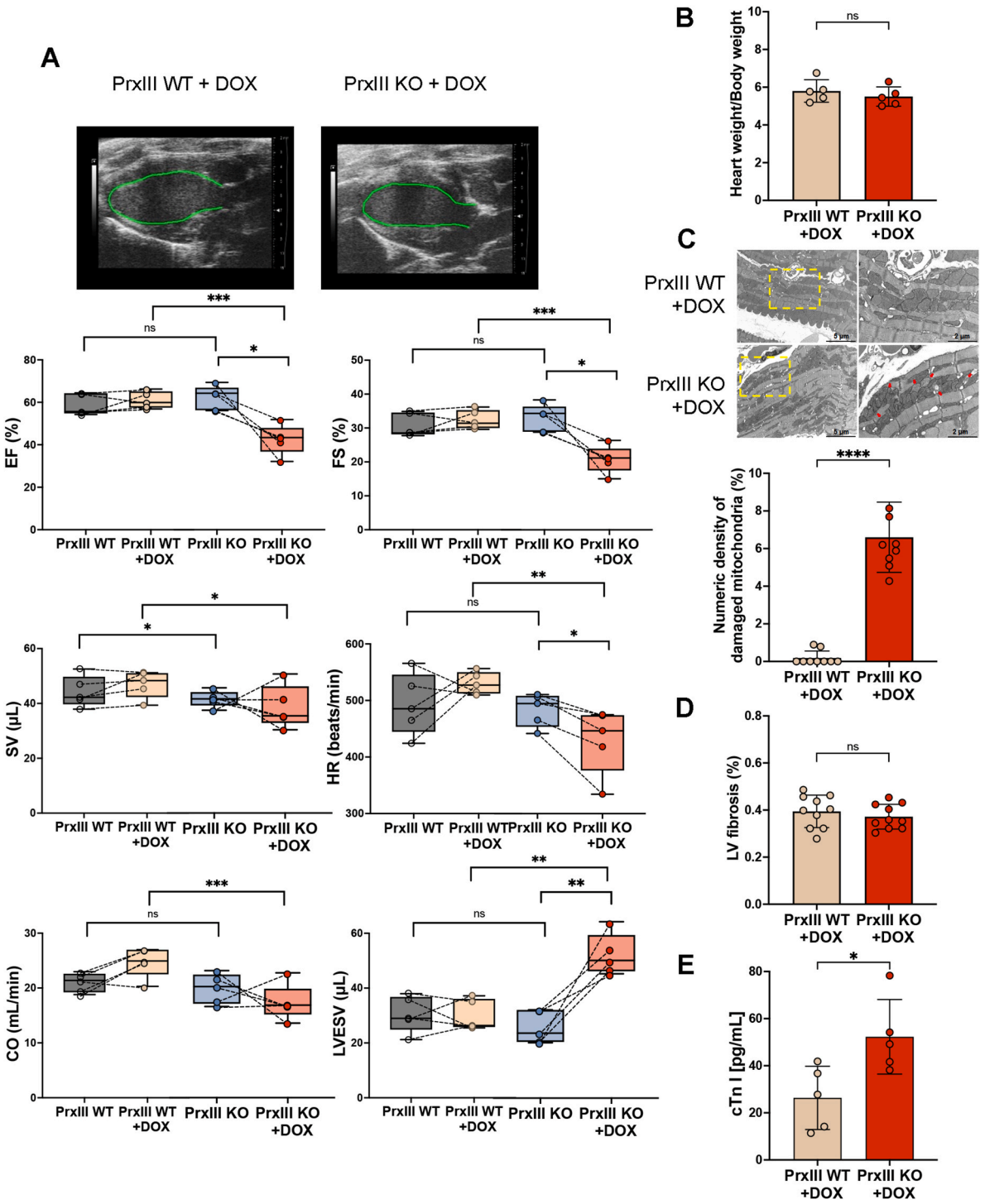


Fig. 9. PrxIII deficiency aggravates DOX-induced cardiac dysfunction and mitochondrial damage *in vivo*.
(A) Longitudinal echocardiographic assessment of cardiac function in wild-type (WT) and PrxIII knockout (KO) mice before and after DOX administration (10 mg/kg, intraperitoneally, 2 weeks). Representative M-mode echocardiographic images from PrxIII WT and KO mice post-DOX are shown (top). Baseline (pre-DOX) and endpoint (post-DOX) measurements of ejection fraction (EF), fractional shortening (FS), heart rate (HR), cardiac output (CO), stroke volume (SV), and left ventricular end-systolic volume (LVESV) are presented as paired before-after plots, with dashed lines connecting individual animals across time points. Within-genotype comparisons (pre-DOX vs. post-DOX) were analyzed by paired Student's t-test, and between-genotype comparisons were analyzed by unpaired Student's t-test ($N = 5$/group). (B) Heart weight/body weight ratio between PrxIII WT and KO mice ($N = 5$/group) post DOX treatment. (C) Representative transmission electron microscopy (TEM) images of cardiac tissue from WT and KO mice post-DOX administration (scale bar, 5 μm for low-magnification images and 2 μm for high-magnification insets). Damaged mitochondria were identified by structural disruption (red arrowheads) and quantified as numeric density. (D) Masson's trichrome staining of LV muscle sections and quantification of cardiac fibrosis in PrxIII WT and KO mice post-DOX administration. Fibrotic area was quantified as a percentage of total tissue area. (E) Serum cTnI levels in PrxIII WT and KO mice post DOX treatment. All data are presented as mean ± S.D. ($N = 5$/group). Statistical significance was determined by Student's t-test. *$p < 0.05$, **$p < 0.01$, ***$p < 0.001$, ****$p < 0.0001$, and ns, $p > 0.05$.

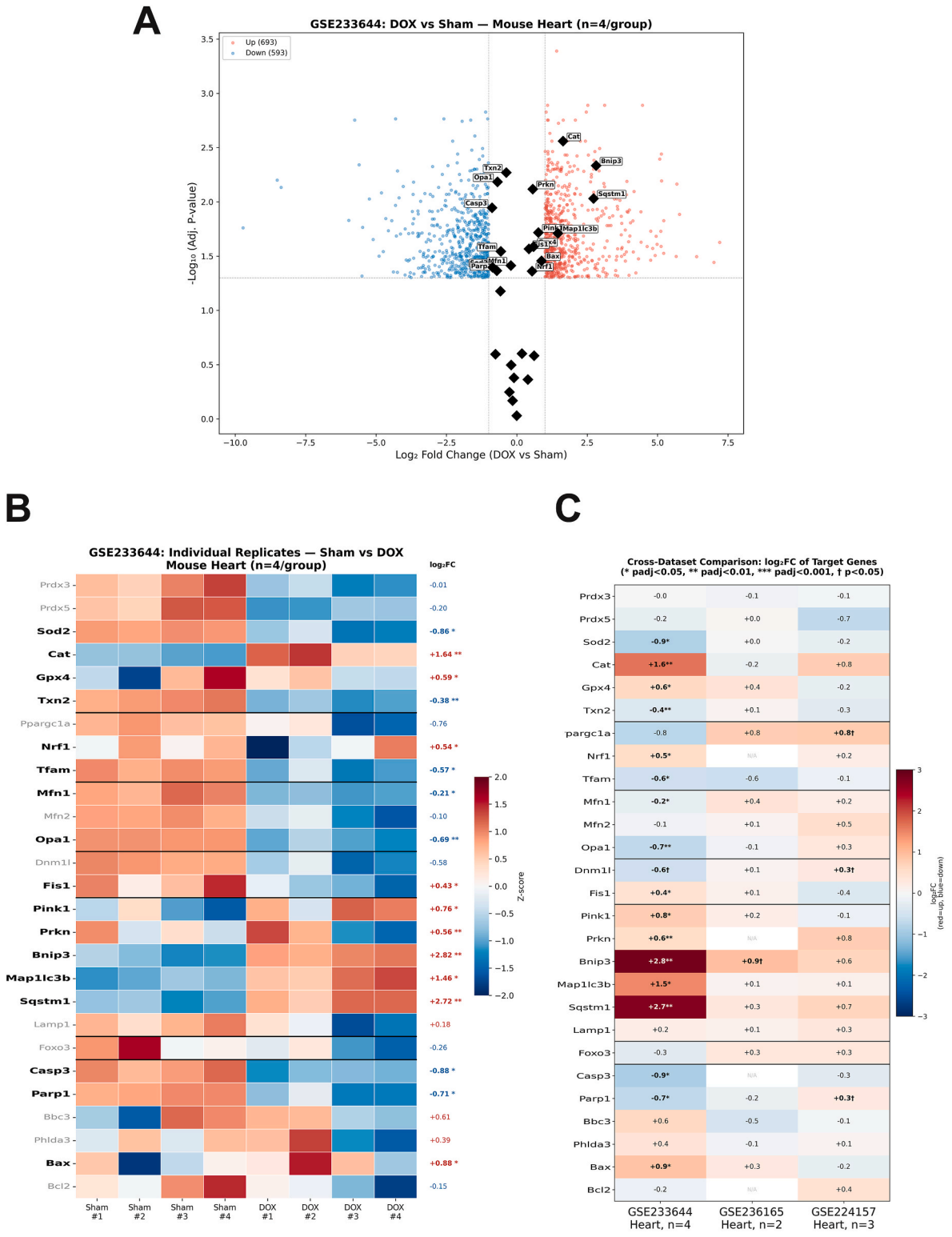


Fig. 10. Bioinformatic analysis of public transcriptome datasets confirms DOX-induced dysregulation of MQC pathways.
(A) Volcano plot of differentially expressed genes (DEGs) in DOX-treated versus sham mouse hearts from publicly available RNA-seq data (GSE233644, n = 4/group). Black diamonds indicate target genes representing MQC pathways examined in this study. Dashed lines indicate significance thresholds ($|\log_2 FC| > 1$ and adjusted p-value <0.05). (B) Heatmap showing Z-score normalized expression of 27 target genes across individual replicates (Sham #1–4 and DOX #1–4) from GSE233644. Genes are grouped by functional pathway category. Bold gene names indicate statistical significance (adjusted $p < 0.05$). $\log_2 FC$ values and significance levels are shown on the right. (C) Cross-dataset comparison of $\log_2 FC$ values for target genes across three independent public DOX cardiotoxicity transcriptome datasets (GSE233644, mouse heart, n = 4; GSE236165, mouse heart, n = 2; GSE224157, mouse heart, n = 3).

These transcriptomic findings from independent public datasets confirm that the core signaling pathways examined in our study — mitophagy, mitochondrial fusion, biogenesis, antioxidant defense, and apoptosis — are indeed dysregulated during DOX-induced cardiotoxicity *in vivo*. Direct validation of these pathway alterations in our own genetic model, including the effect of PrxIII deficiency and SS-31 rescue at the transcriptional level, is presented in the context of the SS-31 rescue experiment below (Fig. 11E–H).

3.11. SS-31, a mitochondria-targeted antioxidant, rescues DOX-induced cardiac dysfunction and mitochondrial injury exacerbated by PrxIII deficiency in vivo

To definitively establish the causal link between mitochondrial H_2O_2 regulation and cardioprotection *in vivo*, we evaluated the therapeutic potential of mitochondria-targeted antioxidants. While triphenyl phosphonium (TPP+)-conjugated antioxidants, such as MitoQ and SKQ1, are extensively utilized, their mitochondrial accumulation strictly depends on a highly negative $\Delta\Psi_m$ [73]. Because DOX treatment severely dissipates $\Delta\Psi_m$, the cellular uptake of these lipophilic cations is intrinsically compromised when they are needed most. Furthermore, under severe oxidative stress, ubiquinone derivatives like MitoQ run the risk of acting as pro-oxidants via redox cycling [74]. In contrast, the mitochondria-targeted peptide, SS-31 selectively localizes to the inner mitochondrial membrane and directly stabilizes cardiolipin in a $\Delta\Psi_m$-independent manner [75,76]. By preserving cardiolipin integrity, SS-31 prevents electron leakage from the respiratory chain and inhibits cytochrome *c* peroxidase activity, thereby effectively suppressing mitochondrial H_2O_2 generation at its source [42,77]. This dual action of attenuating the H_2O_2 burden and protecting the inner membrane makes SS-31 a safer and mechanistically sound alternative.

To empirically validate this rationale, we first conducted a comparative *in vivo* study in WT mice to assess the efficacy and systemic safety of MitoQ, SkQ1, and SS-31 against DOX-induced cardiotoxicity (Supplementary Fig. S2). Echocardiographic analysis revealed that SS-31 administration significantly restored cardiac function, evident in improved EF and FS, whereas MitoQ and SkQ1 failed to provide significant cardioprotection (Supplementary Fig. S2A). Moreover, monitoring of body weight to assess systemic toxicity revealed that mice co-treated with MitoQ and SKQ1 exhibited severe body weight loss (average 4–6 g), indicating substantial systemic toxicity. Conversely, the SS-31-treated group maintained a body weight profile similar to the DOX-alone group, highlighting its superior systemic safety (Supplementary Fig. S2B).

Based on these compelling results, we selected SS-31 to investigate whether protecting the mitochondrial inner membrane could rescue cardiac dysfunction in our PrxIII KO model (Fig. 11). Echocardiographic assessments demonstrated that DOX-induced cardiac dysfunction was profoundly exacerbated in PrxIII KO mice compared to WT mice, as shown by drastic declines in EF, FS, SV, and CO, and alongside LVESV (Fig. 11A). Remarkably, daily SS-31 administration successfully rescued this exacerbated cardiotoxicity in PrxIII KO mice, restoring all functional parameters to levels comparable to or better than those of DOX-treated WT mice. Furthermore, we measured serum cTnI levels to evaluate structural cardiomyocyte injury. Consistent with the functional data, the severely elevated cTnI levels observed in DOX-treated PrxIII KO mice were markedly attenuated by SS-31 treatment (Fig. 11B).

Although TEM imaging of the rescue cohort could not be performed — as cardiac tissues were snap-frozen at −80 °C to preserve utility for protein- and RNA-based biochemical analyses rather than fixed in glutaraldehyde required for ultrastructural preservation — TEM evidence for DOX-induced mitochondrial ultrastructural damage in PrxIII KO hearts is already documented in Fig. 9C, establishing the structural phenotype from which SS-31-mediated rescue is assessed.

To assess mitochondrial structural integrity at the molecular level, we performed immunoblot analysis on cardiac tissue lysates. OPA1, a key inner mitochondrial membrane fusion protein, was analyzed as L-OPA1/S-OPA1 ratio, which reflects the balance between fusion-competent (long) and cleaved (short) forms. The L-OPA1/S-OPA1 ratio was significantly decreased in DOX-treated PrxIII KO hearts compared with control groups, indicating enhanced proteolytic processing of OPA1 under conditions of excessive mitochondrial H_2O_2. SS-31 co-treatment significantly restored the L-OPA1/S-OPA1 ratio in KO mice, suggesting that cardiolipin stabilization by SS-31 protects OPA1 from stress-induced cleavage (Fig. 11C). TOM20, an outer mitochondrial membrane marker reflecting mitochondrial mass, was decreased in DOX-treated hearts, with a more pronounced reduction in PrxIII KO mice. SS-31 treatment partially restored TOM20 levels, indicating preservation of mitochondrial content (Fig. 11C).

Apoptosis markers were also assessed by immunoblot. Bax protein levels were significantly elevated in DOX-treated PrxIII KO hearts. SS-31 co-treatment reduced Bax expression. Cleaved caspase-3, the executioner caspase indicative of active apoptosis, was increased in DOX-treated hearts and further elevated in PrxIII KO mice. SS-31 treatment attenuated cleaved caspase-3 levels, confirming that mitochondria-targeted antioxidant intervention reduces DOX-induced apoptotic signaling (Fig. 11D).

To further validate the rescue effect of SS-31 at the transcriptional level and to confirm concordance with the public transcriptomic data (Fig. 10), we performed qPCR analysis on cardiac tissues from the same cohort of PrxIII WT and KO mice across the three treatment groups. Bnip3 mRNA was significantly elevated in DOX-treated hearts, with a more pronounced increase in PrxIII KO mice, and this elevation was attenuated by SS-31 co-treatment (Fig. 11E). Similarly, Pink1 and Parkin (Prkn) mRNA levels were increased in DOX-treated PrxIII KO hearts compared with WT controls, and SS-31 partially restored these levels (Fig. 11F and G). Bax mRNA showed a significant increase specifically in DOX-treated PrxIII KO hearts, which was significantly reduced by SS-31 (Fig. 11H). Collectively, these qPCR data demonstrate that PrxIII deficiency exacerbates DOX-induced transcriptional activation of mitophagy and apoptosis pathways *in vivo*, and that SS-31 intervention rescues these transcriptional alterations, providing convergent molecular validation fully consistent with the public transcriptome data (Fig. 10) and our *in vitro* mechanistic findings.

These data demonstrate that SS-31 effectively rescues DOX-induced cardiac dysfunction and mitigates molecular markers of mitochondrial structural compromise and apoptosis in PrxIII KO hearts. These findings establish that mitochondria-targeted cardiolipin stabilization can functionally compensate for the loss of PrxIII-mediated H_2O_2 detoxification, reinforcing the central role of mitochondrial oxidative stress in DOX-induced cardiotoxicity.

4. Discussion

In this study, we utilized rat cardiomyocytes with altered expression levels of mitochondrial antioxidant enzyme PrxIII to elucidate the specific role of mitochondrial H_2O_2 levels in DOX-induced cardiotoxicity. PrxIII is exclusively localized to mitochondria and is primarily responsible for detoxifying mitochondrial H_2O_2. Unlike catalase or Gpx, which act in other cellular compartments, PrxIII directly removes H_2O_2 within the matrix with high catalytic efficiency and thus defines the physiological redox set-point of mitochondria [17]. Among mitochondrial ROS, H_2O_2 exhibits high membrane permeability and can diffuse throughout the cell, generating hydroxy radicals via the Fenton reaction and amplifying oxidative damage [15]. Hence, our findings specifically highlighted mitochondrial H_2O_2 as a critical mediator of DOX-induced cardiac injury.

DOX-induced cardiotoxicity occurs primarily through mitochondrial oxidative stress, initiated by accumulation of DOX in the mitochondrial inner membrane, generating superoxide radicals ($O_2\bullet^-$) via electron leakage from the ETC [78]. $O_2\bullet^-$ is rapidly converted to H_2O_2 by mitochondrial superoxide dismutase (SOD2), leading to oxidative

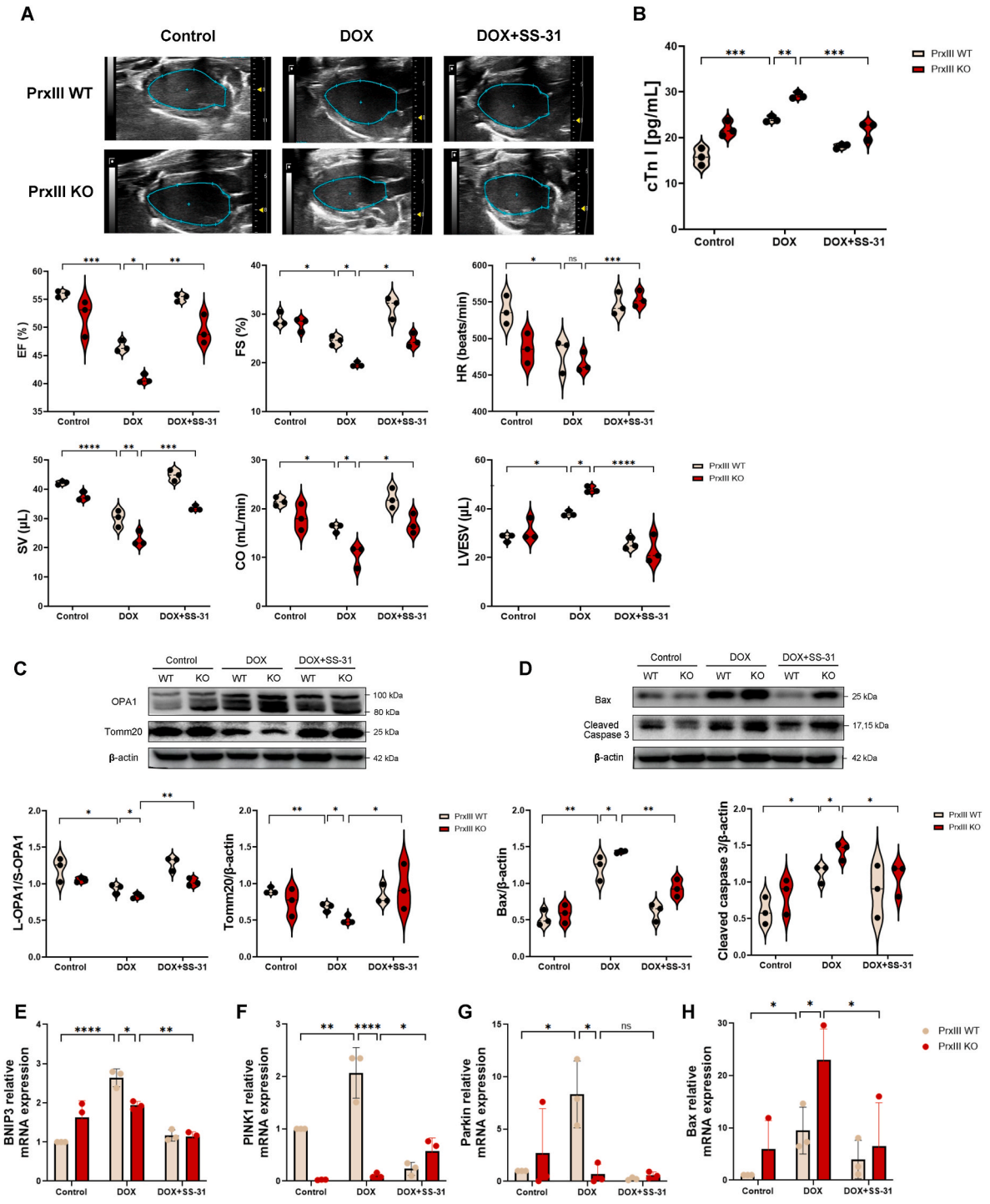


Fig. 11. SS-31 rescues DOX-induced cardiac dysfunction and mitochondrial injury exacerbated by PrxIII deficiency *in vivo*.
(A) Analysis of cardiac function using echocardiography in wild-type (WT) and PrxIII knockout (KO) mice. Mice were treated with PBS (Control), DOX (5 mg/kg/week, intraperitoneally, 4 weeks) alone, or DOX combined with daily administration of the mitochondria-targeted peptide SS-31 (3 mg/kg/day, intraperitoneally) in a complete 3 × 2 factorial design (N = 3/group). Representative M-mode echocardiographic images (top) and quantification of ejection fraction (EF), fractional shortening (FS), heart rate (HR), cardiac output (CO), stroke volume (SV), and left ventricular end-systolic volume (LVESV) are shown. (B) Serum cTnI levels across all six groups. (C, D) Cardiac tissue lysates were subjected to immunoblot analyses for OPA1 and Tomm20 (C) and Bax and cleaved Caspase-3 (D), with β-actin as a loading control. For OPA1, the L-OPA1/S-OPA1 ratio was quantified as a functional indicator of mitochondrial inner membrane integrity and fusion competence; TOMM20, Bax, and cleaved caspase-3 were each normalized to β-actin. Densitometric quantification was performed from three independent biological replicates. (E–H) qPCR validation of selected mitophagy and apoptosis markers in cardiac tissues from PrxIII WT and KO mice across the three treatment groups. (E) Bnip3 mRNA expression. (F) Pink1 mRNA expression. (G) Parkin (Prkn) mRNA expression. (H) Bax mRNA expression. All data are presented as violin plots showing the median and quartiles (N = 3/group). Statistical analysis was performed using two-way ANOVA with Tukey's post-hoc test. *$p < 0.05$, **$p < 0.01$, ***$p < 0.001$, ****$p < 0.0001$, and ns, $p > 0.05$.

damage within mitochondria. Increased mitochondrial H_2O_2 levels induce cardiolipin oxidation, critically damaging the mitochondrial inner membrane. Consistent with this, we observed significantly elevated mitochondrial H_2O_2 and exacerbated cardiolipin oxidation after DOX treatment in PrxIII-depleted cells compared to controls. Cardiolipin plays essential roles in ATP-synthase assembly and the formation of mitochondrial permeability transition pore (mPTP), the opening of which leads to loss of $\Delta\Psi_m$ and initiation of apoptosis [44]. Our data clearly demonstrated greater $\Delta\Psi_m$ dissipation in PrxIII-depleted cells following DOX treatment, underscoring the importance of PrxIII in mitochondrial membrane protection. Beyond morphological changes, we confirmed that excessive mitochondrial H_2O_2 leads to bioenergetic collapse. PrxIII depletion significantly reduced ATP production and OCR, demonstrating that PrxIII-mediated redox buffering preserves oxidative phosphorylation and prevents respiratory failure.

Recently, MQC mechanisms, including mitochondrial biogenesis, mitochondrial dynamics (fusion and fission) and mitophagy, have gained considerable attention as critical regulators of mitochondrial function and cellular survival under stress conditions [22,79,80]. We found that PrxIII deficiency suppressed the biosynthetic arm of MQC. Expression of PGC-1α, Nrf1, and mtTFA was markedly reduced, accompanied by decreased mtDNA-encoded cytochrome *c* oxidase transcripts. Interestingly, PGC-1α exhibited a biphasic response to DOX-induced oxidative stress: moderate mitochondrial H_2O_2 in control cells transiently up-regulated PGC-1α, representing an adaptive transcriptional attempt to reinforce mitochondrial renewal, whereas excessive mitochondrial H_2O_2 in PrxIII-deficient cells led to pronounced decline in both PGC-1α expression and protein stability, accompanied by broad suppression of downstream biogenic genes. This apparent discrepancy reflects the temporal and redox-sensitive nature of the PGC-1α signaling cascade. PGC-1α is rapidly activated through post-translational modifications [48,81,82], but sustained induction of its targets requires stable redox homeostasis and intact nuclear-mitochondrial communication. Moreover, excessive ROS can directly compromise the stability or activity of NRF1 and TFAM proteins via oxidative modification [83,84] or p53-mediated transcriptional repression [85,86], further blocking the biogenic program. Thus, PrxIII functions as a pivotal redox buffer that preserves the mitochondrial biogenesis axis.

Mitochondria balance between fusion and fission maintains mitochondrial homeostasis by repairing or removing damaged mitochondria [87]. However, the change of mitochondrial dynamics in DOX-induced cardiotoxicity remains controversial [9,27,88,89]. Here, we clearly demonstrated that PrxIII depletion leads to excessive mitochondrial H_2O_2 accumulation, which subsequently impairs mitochondrial fusion by reducing the expression of fusion proteins (Mfn1, Mfn2, and OPA1). Conversely, moderate mitochondrial H_2O_2 levels induced by DOX in PrxIII-expressing cells enhanced the expression of these fusion proteins. Notably, OPA1 expression exhibited the most prominent change, potentially due to its crucial role in inner mitochondrial membrane fusion, closely interacting with cardiolipin [90–92]. In contrast, mitochondrial fission, mediated by a GTPase called Drp1, facilitates removal of irreversibly damaged mitochondria. Drp1 activity is regulated by post-translational modifications, particularly phosphorylation at Ser616, enhancing Drp1 oligomerization and mitochondrial fission [93,94]. Our study observed reduced Drp1 phosphorylation upon DOX treatment, suggesting impaired mitochondrial fission. However, Drp1 phosphorylation was unaffected by PrxIII depletion, indicating mitochondrial fusion may be more sensitive to changes in mitochondrial H_2O_2 compared to fission under DOX-induced stress conditions.

Autophagy is an indispensable catabolic process that degrades cytoplasmic material and damaged organelles, such as mitochondria or protein aggregates, thus maintaining cell survival [56,95]. Under normal physiological conditions, autophagy proceeds efficiently, removing dysfunctional mitochondria and preventing excessive ROS production [61]. However, when lysosomal function is compromised, autophagic flux is impaired, leading to cellular damage. Even when autophagy is excessive, cell death can increase as important cell components are removed [66,96]. Recent studies showed that excessive ROS impairs autophagy initiation by oxidizing Atg proteins [97] and disrupting lysosomal acidification [61,62]. In our study, we clearly showed that PrxIII depletion-induced excessive mitochondrial H_2O_2 accumulation markedly impaired autophagosome formation and autophagic flux through lysosomal dysfunction, while moderate H_2O_2 facilitated autophagic flux as an adaptive response. Interestingly, previous reports have shown that DOX affects autophagic flux in a dose-dependent manner. Low doses or early phases of DOX treatment activate autophagy, whereas large doses or late phases of DOX treatment inhibit autophagy, both inducing cellular death [36]. Our current results align with these observations, demonstrating that mitochondrial H_2O_2 levels can explain this dose-dependent regulation of autophagy by DOX. While we elucidated lysosomal blockage and autophagic flux damage, autophagy initiation and the effects of mitochondrial H_2O_2 on Atg proteins require further research.

Mitophagy is a specialized form of selective autophagy that specifically targets damaged mitochondria for degradation, thereby maintaining mitochondrial quality and cellular homeostasis. Mitophagy initiation involves recognition of damaged mitochondria, followed by their sequestration into autophagosomes and subsequent fusion with lysosomes for degradation. Two major pathways have been widely studied to mediate this selective mitochondrial clearance: the ubiquitin-dependent PTEN-induced kinase 1 (PINK1)/Parkin pathway and the ubiquitin-independent receptor-mediated mitophagy pathway [9,98]. In our study, we specifically investigated mitophagy by analyzing PINK1/Parkin as the representative ubiquitin-dependent pathway and BNIP3 as the representative receptor-mediated pathway to comprehensively understand how mitochondrial H_2O_2 accumulation under DOX-induced oxidative stress modulates selective mitochondrial removal. BNIP3 has been previously identified as highly responsive to oxidative stress conditions, including those induced by DOX [99,100], and is linked functionally to the PINK1/Parkin pathway through regulation of PINK1 stability and cleavage [101]. Furthermore, transcription control of both the PINK1/parkin and BNIP3 pathways via the FOXO3a transcription factor further underscores their coordinated regulation under oxidative stress conditions [88,93]. Thus, by focusing on these two critical mitophagy parameters –PINK1/Parkin and BNIP3– we provide comprehensive mechanistic insight into MQC under varying mitochondrial H_2O_2 stress conditions induced by DOX treatment. Our findings clearly demonstrate how differing mitochondrial H_2O_2 levels distinctly modulate mitophagy pathways, revealing adaptive versus maladaptive mitochondrial responses to DOX-induced cardiotoxicity.

Our *in vivo* findings translate the mechanistic framework established *in vitro* into physiologically relevant cardiac pathology. Critically, the pattern of injury in PrxIII KO mice — pronounced systolic dysfunction and mitochondrial ultrastructural damage occurring in the absence of concurrent hypertrophic remodeling or fibrosis — argues that the primary driver of cardiac dysfunction is acute mitochondrial quality failure rather than chronic structural remodeling. This distinction carries important clinical significance: it suggests that the pathological cascade leading to overt heart dysfunction may be reversible at an early stage, before fibrotic changes become irreversible, provided that mitochondrial oxidative stress is appropriately controlled. The temporal concordance between echocardiographic decline and mitochondrial structural deterioration — without accompanying fibrosis — further supports the *in vitro* finding that excessive mitochondrial H_2O_2 is sufficient to drive cardiomyocyte dysfunction independently of extracellular matrix pathology.

The transcriptomic data provide an additional layer of interpretive significance beyond mere pathway confirmation. The consistent directionality of mitophagy, mitochondrial fusion, biogenesis, and apoptosis gene dysregulation across three independent public DOX cardiotoxicity datasets — spanning different DOX regimens, time points, and animal

cohorts — demonstrates that the pathway alterations identified in PrxIII-depleted cardiomyocytes are not artifacts of the *in vitro* system, but reflect core transcriptional responses to DOX-induced mitochondrial oxidative stress that are conserved across experimental contexts. Furthermore, the amplification of these transcriptional changes in PrxIII KO hearts (Fig. 11E–H), together with their attenuation by SS-31, establishes PrxIII as a molecular gatekeeper whose enzymatic activity directly determines the amplitude and reversibility of the transcriptional stress response to DOX.

The molecular data from the SS-31 rescue experiment reveal a mechanistically coherent chain of protection that extends beyond simple ROS scavenging. The restoration of the L-OPA1/S-OPA1 ratio by SS-31 is particularly informative: OPA1 cleavage from its fusion-competent long form (L-OPA1) to the short form (S-OPA1) is mediated by the stress-activated inner membrane protease OMA1, which is potently activated by oxidative stress and $\Delta\Psi_m$ dissipation [102,103]. Of particular mechanistic relevance, inactivation of PrxIII has been shown to directly correlate with OMA1 activation and OPA1 processing [102], consistent with the notion that loss of PrxIII-mediated H_2O_2 detoxification creates a permissive redox environment for OMA1 hyperactivation and consequent inner membrane structural remodeling. By stabilizing cardiolipin directly, SS-31 interrupts this upstream trigger of OMA1 activation, thereby preserving OPA1 in its fusion-competent state rather than simply scavenging H_2O_2 after oxidative damage has already propagated. This positions cardiolipin integrity as the critical upstream determinant of cristae architecture and mitochondrial fusion competence — consistent with our *in vitro* finding that OPA1 exhibited the most prominent and DOX-sensitive change among all fusion proteins examined. The partial restoration of TOM20 further suggests that SS-31 not only arrests ongoing mitochondrial loss but may also relieve the excessive mitophagic clearance driven by PINK1/Parkin and BNIP3 pathway activation, allowing partial recovery of mitochondrial mass. The attenuation of Bax and cleaved caspase-3 confirms that this structural stabilization propagates downstream to suppress apoptotic commitment.

Collectively, these observations demonstrate that targeting the cardiolipin–OPA1 axis at the inner membrane can functionally substitute for the upstream enzymatic H_2O_2-detoxification capacity of PrxIII, even in its complete absence. This mechanistic equivalence has direct translational relevance: elamipretide (SS-31) has already demonstrated cardioprotective potential in multiple preclinical models and has entered clinical evaluation [104], and our findings provide a specific mechanistic rationale for its potential utility in anthracycline-induced cardiotoxicity, particularly in patients whose mitochondrial antioxidant capacity may be constitutively reduced by genetic variation, aging, or comorbid conditions.

In summary, our study conclusively demonstrated that precise mitochondrial H_2O_2 regulation through the mitochondrial antioxidant enzyme PrxIII plays a critical protective role against DOX-induced mitochondrial dysfunction, impaired MQC, and apoptosis in cardiomyocytes. Importantly, the present study identifies the redox-sensitive transcription factor FOXO3a as a molecular switch that links mitochondrial H_2O_2 levels to divergent cellular responses [40,105,106]. Moderate increases in mitochondrial H_2O_2 in PrxIII-expressing cells promoted nuclear translocation of FOXO3a [107,108], consistent with activation of antioxidant and mitophagy-related genes that enhance mitochondrial turnover. Conversely, excessive H_2O_2 accumulation in PrxIII-deficient cells disrupted FOXO3a nuclear localization, likely due to irreversible oxidative modification [109] or phosphorylation by stress kinases [110], thereby preventing activation of adaptive programs. Consequently, the cellular response shifts from adaptive to maladaptive, transitioning from redox signaling to oxidative injury. This duality provides a mechanistic explanation for how moderate versus excessive H_2O_2 levels produce fundamentally different outcomes—adaptive redox signaling versus aggressive oxidative stress—under DOX treatment.

The clear cause-effect relationships established here highlight mitochondrial H_2O_2 as a central regulatory node controlling mitochondrial dynamics and mitophagy. Thus, therapeutic strategies aiming to enhance mitochondrial antioxidant capacity or directly targeting mitochondrial oxidative stress pathways—such as mitochondria-targeted antioxidants (e.g., MitoQ, SkQ1, or SS-31)—may offer promising approaches to mitigate DOX-induced cardiotoxicity [36,111]. These findings not only firmly link the preservation of mitochondrial structural integrity to cardioprotection but also provide direct evidence that targeting mitochondrial oxidative stress is a highly efficacious clinical strategy [112]. Further exploration and clinical validation of these mitochondrial-targeted interventions could lead to significantly improved cardioprotective outcomes in patients undergoing chemotherapy with DOX.

5. Conclusions

Our study provides important insight into how mitochondrial H_2O_2 critically influences DOX-induced cardiac toxicity through differential regulation of mitochondrial dynamics and mitophagy. Specifically, we demonstrate that mitochondrial H_2O_2 acts as a crucial upstream mediator determining the functional outcomes of the MQC system under DOX-induced stress conditions. Under moderate mitochondrial oxidative stress, mitochondrial fusion and mitophagy processes are activated as adaptive responses, facilitating efficient removal or repair of damaged mitochondria and thereby preserving cardiomyocyte homeostasis. However, severe oxidative stress conditions, as observed in PrxIII-depleted cardiomyocytes exposed to DOX, cause substantial decline of mitochondrial biogenesis, impairment of mitochondrial fusion, significantly reduce mitophagy capacity, and disrupt lysosome function, collectively blocking autophagic flux. Consequently, such severe mitochondrial oxidative stress conditions trigger profound mitochondrial damage and eventually apoptotic cell death. Thus, our findings clearly establish a direct cause-effect relationship between mitochondrial H_2O_2 levels and MQC function, providing critical evidence that maintaining appropriate mitochondrial H_2O_2 levels through antioxidant systems, particularly PrxIII, is essential for cardiomyocyte protection against DOX-induced oxidative stress and mitochondrial dysfunction. Targeting mitochondrial H_2O_2 levels and enhancing mitochondrial antioxidant capacity, therefore, represent a promising therapeutic strategy for mitigating DOX-induced cardiotoxicity.

Funding

This work was supported by the National Research Foundation of Korea (NRF) grant funded by the Ministry of Science and ICT (MSIT) (NRF-2020R1A2C1006443), the Basic Science Research Program through the National Research Foundation of Korea funded by the Ministry of Education (NRF-2022R1A6A1A03046247), and the Brain Korea 21 Plus Program funded by the Korean government (MOE) in the Republic of Korea.

CRediT authorship contribution statement

Ji Won Park: Conceptualization, Data curation, Formal analysis, Methodology, Visualization, Writing – original draft, Writing – review & editing. **Se Yeon Jang:** Conceptualization, Formal analysis, Investigation, Methodology, Software. **Mi Yeon Kim:** Conceptualization, Formal analysis, Investigation, Methodology, Software. **Ho Jin Yi:** Formal analysis, Methodology, Visualization. **Seong Keun Sonn:** Formal analysis, Methodology, Visualization. **Okhee Kweon:** Methodology, Visualization. **Byung-Hoon Lee:** Methodology, Resources, Validation. **Goo Taeg Oh:** Methodology, Resources, Validation. **Hyun Ae Woo:** Conceptualization, Methodology, Project administration, Resources, Supervision. **Tong-Shin Chang:** Conceptualization, Funding acquisition, Methodology, Project administration, Resources, Supervision.

Declaration of competing interest

The authors declare that they have no known competing financial interests or personal relationships that could have appeared to influence the work reported in this paper.

Appendix A. Supplementary data

Supplementary data to this article can be found online at https://doi.org/10.1016/j.redox.2026.104176.

Data availability

Data will be made available on request.

References

[1] F. Yang, et al., Doxorubicin, DNA torsion, and chromatin dynamics, Biochim. Biophys. Acta Rev. Canc 1845 (1) (2014) 84–89.
[2] S.Y. van der Zanden, X. Qiao, J. Neefjes, New insights into the activities and toxicities of the old anticancer drug doxorubicin, FEBS J. 288 (21) (2021) 6095–6111.
[3] L.E. Wold, N.S. Aberle 2nd, J. Ren, Doxorubicin induces cardiomyocyte dysfunction via a p38 MAP kinase-dependent oxidative stress mechanism, Cancer Detect. Prev. 29 (3) (2005) 294–299.
[4] G. Capranico, F. Zunino, DNA topoisomerase-trapping antitumour drugs, Eur. J. Cancer 28 (12) (1992) 2055–2060.
[5] Q. Xiong, et al., Proteasomes of autophagy-deficient cells exhibit alterations in regulatory proteins and a marked reduction in activity, Cells 12 (11) (2023).
[6] R.A. Minow, et al., Adriamycin cardiomyopathy—risk factors, Cancer 39 (4) (1977) 1397–1402.
[7] S. Zhou, et al., Cumulative and irreversible cardiac mitochondrial dysfunction induced by doxorubicin, Cancer Res. 61 (2) (2001) 771–777.
[8] J. Doroshow, K. Davies, Redox cycling of anthracyclines by cardiac mitochondria. II. Formation of superoxide anion, hydrogen peroxide, and hydroxyl radical, J. Biol. Chem. 261 (7) (1986) 3068–3074.
[9] S. Antonucci, F. Di Lisa, N. Kaludercic, Mitochondrial reactive oxygen species in physiology and disease, Cell Calcium 94 (2021) 102344.
[10] E. Goormaghtigh, et al., Structure of the adriamycin-cardiolipin complex: role in mitochondrial toxicity, Biophys. Chem. 35 (2–3) (1990) 247–257.
[11] B. Kalyanaraman, J.J. Shashi Kalivendi, Suwei Wang, E.K.a.S. Kotamraju, Doxorubicin-induced apoptosis: implications in cardiotoxicity, Mol. Cell. Biochem. (2002).
[12] H. Mizutani, et al., Distinct mechanisms of site-specific oxidative DNA damage by doxorubicin in the presence of copper (II) and NADPH-cytochrome P450 reductase, Cancer Sci. 94 (8) (2003) 686–691.
[13] G.S. Shadel, T.L. Horvath, Mitochondrial ROS signaling in organismal homeostasis, Cell 163 (3) (2015) 560–569.
[14] M. Giorgio, et al., Hydrogen peroxide: a metabolic by-product or a common mediator of ageing signals? Nat. Rev. Mol. Cell Biol. 8 (9) (2007) 722–728.
[15] I.A. Rukavina-Mikusic, et al., Mitochondrial H(2)O(2) metabolism as central event of heart complex I syndrome in early diabetes, Free Radic. Biol. Med. 201 (2023) 66–75.
[16] T.S. Chang, et al., Peroxiredoxin III, a mitochondrion-specific peroxidase, regulates apoptotic signaling by mitochondria, J. Biol. Chem. 279 (40) (2004) 41975–41984.
[17] Andrew G. Cox, Christine C. Winterbourn, Mark B. Hampton, Mitochondrial peroxiredoxin involvement in antioxidant defence and redox signalling, Biochem. J. 425 (2) (2009) 313–325.
[18] J.Y. Baek, et al., Protective role of mitochondrial Peroxiredoxin III against UVB-Induced apoptosis of epidermal keratinocytes, J. Invest. Dermatol. 137 (6) (2017) 1333–1342.
[19] P.S. Rawat, et al., Doxorubicin-induced cardiotoxicity: an update on the molecular mechanism and novel therapeutic strategies for effective management, Biomed. Pharmacother. 139 (2021) 111708.
[20] S.R. Kim, et al., Mitochondrial H(2)O(2) is a central mediator of diclofenac-induced hepatocellular injury, Antioxidants 13 (1) (2023).
[21] O. Abu Shelbayeh, et al., PGC-1alpha is a master regulator of mitochondrial lifecycle and ROS stress response, Antioxidants 12 (5) (2023).
[22] H.M. Ni, J.A. Williams, W.X. Ding, Mitochondrial dynamics and mitochondrial quality control, Redox Biol. 4 (2015) 6–13.
[23] D.C. Chan, Mitochondrial dynamics and its involvement in disease, Annu. Rev. Pathol. 15 (2020) 235–259.
[24] M. Tong, J. Sadoshima, Mitochondrial autophagy in cardiomyopathy, Curr. Opin. Genet. Dev. 38 (2016) 8–15.
[25] J.E. Dominy, P. Puigserver, Mitochondrial biogenesis through activation of nuclear signaling proteins, Cold Spring Harbor Perspect. Biol. 5 (7) (2013).
[26] R.J. Youle, A.M. Van Der Bliek, Mitochondrial fission, fusion, and stress, Science 337 (6098) (2012) 1062–1065.
[27] M.P. Catanzaro, et al., Doxorubicin-induced cardiomyocyte death is mediated by unchecked mitochondrial fission and mitophagy, FASEB J. 33 (10) (2019) 11096–11108.
[28] L.H.H. Aung, et al., Cardiomyocyte mitochondrial dynamic-related lncRNA 1 (CMDL-1) may serve as a potential therapeutic target in doxorubicin cardiotoxicity, Mol. Ther. Nucleic Acids 25 (2021) 638–651.
[29] N. Osataphan, et al., Effects of doxorubicin-induced cardiotoxicity on cardiac mitochondrial dynamics and mitochondrial function: insights for future interventions, J. Cell Mol. Med. 24 (12) (2020) 6534–6557.
[30] S.H. Jung, et al., Diclofenac impairs autophagic flux via oxidative stress and lysosomal dysfunction: implications for hepatotoxicity, Redox Biol. 37 (2020) 101751.
[31] B.C. Dickinson, V.S. Lin, C.J. Chang, Preparation and use of MitoPY1 for imaging hydrogen peroxide in mitochondria of live cells, Nat. Protoc. 8 (6) (2013) 1249–1259.
[32] M.I. Garcia Fernandez, D. Ceccarelli, U. Muscatello, Use of the fluorescent dye 10-N-nonyl acridine orange in quantitative and location assays of cardiolipin: a study on different experimental models, Anal. Biochem. 328 (2) (2004) 174–180.
[33] A.J. Valente, et al., A simple ImageJ macro tool for analyzing mitochondrial network morphology in mammalian cell culture, Acta Histochem. 119 (3) (2017) 315–326.
[34] S.R. Yoshii, N. Mizushima, Monitoring and measuring autophagy, Int. J. Mol. Sci. 18 (9) (2017).
[35] S.K. Sonn, et al., Peroxiredoxin 3 deficiency induces cardiac hypertrophy and dysfunction by impaired mitochondrial quality control, Redox Biol. 51 (2022) 102275.
[36] K.B. Wallace, V.A. Sardao, P.J. Oliveira, Mitochondrial determinants of doxorubicin-induced cardiomyopathy, Circ. Res. 126 (7) (2020) 926–941.
[37] B. Kalyanaraman, et al., Measuring reactive oxygen and nitrogen species with fluorescent probes: challenges and limitations, Free Radic. Biol. Med. 52 (1) (2012) 1–6.
[38] S.J. Jeong, J.G. Park, G.T. Oh, Peroxiredoxins as potential targets for cardiovascular disease, Antioxidants 10 (8) (2021).
[39] L.O. Klotz, et al., Redox regulation of FoxO transcription factors, Redox Biol. 6 (2015) 51–72.
[40] C. Fasano, et al., FOXO3a from the nucleus to the mitochondria: a round trip in cellular stress response, Cells 8 (9) (2019).
[41] E. Mileykovskaya, W. Dowhan, Cardiolipin-dependent formation of mitochondrial respiratory supercomplexes, Chem. Phys. Lipids 179 (2014) 42–48.
[42] A.V. Birk, et al., The mitochondrial-targeted compound SS-31 re-energizes ischemic mitochondria by interacting with cardiolipin, J. Am. Soc. Nephrol. 24 (8) (2013) 1250–1261.
[43] J. Dudek, Role of cardiolipin in mitochondrial signaling pathways, Front. Cell Dev. Biol. 5 (2017) 90.
[44] G. Paradies, et al., Role of cardiolipin in mitochondrial function and dynamics in health and disease: molecular and pharmacological aspects, Cells 8 (7) (2019).
[45] S.W. Perry, et al., Mitochondrial membrane potential probes and the proton gradient: a practical usage guide, Biotechniques 50 (2) (2011) 98–115.
[46] B.P. Dranka, et al., Assessing bioenergetic function in response to oxidative stress by metabolic profiling, Free Radic. Biol. Med. 51 (9) (2011) 1621–1635.
[47] L.D. Popov, Mitochondrial biogenesis: an update, J. Cell Mol. Med. 24 (9) (2020) 4892–4899.
[48] P.J. Fernandez-Marcos, J. Auwerx, Regulation of PGC-1alpha, a nodal regulator of mitochondrial biogenesis, Am. J. Clin. Nutr. 93 (4) (2011) 884S, 90.
[49] L. Chen, et al., PGC-1alpha-Mediated mitochondrial quality control: molecular mechanisms and implications for heart failure, Front. Cell Dev. Biol. 10 (2022) 871357.
[50] C.A. Piantadosi, H.B. Suliman, Mitochondrial transcription factor A induction by redox activation of nuclear respiratory factor 1, J. Biol. Chem. 281 (1) (2006) 324–333.
[51] M.I. Ekstrand, et al., Mitochondrial transcription factor A regulates mtDNA copy number in mammals, Hum. Mol. Genet. 13 (9) (2004) 935–944.
[52] J.Y. Jin, et al., Drp1-dependent mitochondrial fission in cardiovascular disease, Acta Pharmacol. Sin. 42 (5) (2021) 655–664.
[53] S. Kageyama, et al., p62/SQSTM1-droplet serves as a platform for autophagosome formation and anti-oxidative stress response, Nat. Commun. 12 (1) (2021) 16.
[54] X.J. Zhang, et al., Why should autophagic flux be assessed? Acta Pharmacol. Sin. 34 (5) (2013) 595–599.
[55] R. Wang, et al., Molecular basis of V-ATPase inhibition by bafilomycin A1, Nat. Commun. 12 (1) (2021) 1782.
[56] K.R. Parzych, D.J. Klionsky, An overview of autophagy: morphology, mechanism, and regulation, Antioxidants Redox Signal. 20 (3) (2014) 460–473.
[57] B. Levine, G. Kroemer, Biological functions of autophagy genes: a disease perspective, Cell 176 (1–2) (2019) 11–42.
[58] S. Pickles, P. Vigié, R.J. Youle, Mitophagy and quality control mechanisms in mitochondrial maintenance, Curr. Biol. 28 (4) (2018) R170–R185.
[59] K.K. Mahapatra, et al., The lysosome as an imperative regulator of autophagy and cell death, Cell. Mol. Life Sci. 78 (23) (2021) 7435–7449.
[60] A. Ballabio, J.S. Bonifacino, Lysosomes as dynamic regulators of cell and organismal homeostasis, Nat. Rev. Mol. Cell Biol. 21 (2) (2020) 101–118.
[61] Y. Zhan, et al., Berbamine hydrochloride inhibits lysosomal acidification by activating Nox 2 to potentiate chemotherapy-induced apoptosis via the ROS-MAPK pathway in human lung carcinoma cells, Cell Biol. Toxicol. 39 (4) (2023) 1297–1317.

[62] R. Shyam, et al., Mitochondrial ROS induced lysosomal dysfunction and autophagy impairment in an animal model of congenital hereditary endothelial dystrophy, Investig. Ophthalmol. Vis. Sci. 62 (12) (2021) 15.
[63] R. Marwaha, M. Sharma, DQ-Red BSA trafficking assay in cultured cells to assess cargo delivery to lysosomes, Bio Protoc 7 (19) (2017).
[64] B.W. Dinghuan Deng, Guan Youchen, Zheng Hui, Mutlu Ayse Sena, C. Wang Meng, Quantitative profiling of lysosomal pH heterogeneity using fluorescence lifetime imaging microscopy, bioRxiv (2023).
[65] N.J. Dolman, et al., Tools and techniques to measure mitophagy using fluorescence microscopy, Autophagy 9 (11) (2013) 1653–1662.
[66] S. Ikeda, D. Zablocki, J. Sadoshima, The role of autophagy in death of cardiomyocytes, J. Mol. Cell. Cardiol. 165 (2022) 1–8.
[67] C.C. Wu, S.B. Bratton, Regulation of the intrinsic apoptosis pathway by reactive oxygen species, Antioxidants Redox Signal. 19 (6) (2013) 546–558.
[68] E.B. Affar, et al., Caspase-3-mediated processing of poly(ADP-ribose) glycohydrolase during apoptosis, J. Biol. Chem. 276 (4) (2001) 2935–2942.
[69] A. Strasser, L. O'Connor, V.M. Dixit, Apoptosis signaling, Annu. Rev. Biochem. 69 (2000) 217–245.
[70] A.K. Hammill, J.W. Uhr, R.H. Scheuermann, Annexin V staining due to loss of membrane asymmetry can be reversible and precede commitment to apoptotic death, Exp. Cell Res. 251 (1) (1999) 16–21.
[71] A.S.J. Luciano Babuin, Troponin: the biomarker of choice for the detection of cardiac injury, CMA 173 (10) (2005) 1191.
[72] E.J.S. Denessen, et al., Circulating forms of cardiac troponin: a review with implications for clinical practice, J. Laboratory Precis. Med. 8 (2023), 13-13.
[73] M.P. Murphy, Targeting lipophilic cations to mitochondria, Biochim. Biophys. Acta 1777 (7–8) (2008) 1028–1031.
[74] A.K. Doughan, S.I. Dikalov, Mitochondrial redox cycling of mitoquinone leads to superoxide production and cellular apoptosis, Antioxidants Redox Signal. 9 (11) (2007) 1825–1836.
[75] D.A. Thomas, et al., Mitochondrial targeting with antioxidant peptide SS-31 prevents mitochondrial depolarization, reduces islet cell apoptosis, increases islet cell yield, and improves posttransplantation function, J. Am. Soc. Nephrol. 18 (1) (2007) 213–222.
[76] M.P. Siegel, et al., Mitochondrial-targeted peptide rapidly improves mitochondrial energetics and skeletal muscle performance in aged mice, Aging Cell 12 (5) (2013) 763–771.
[77] H.H. Szeto, First-in-class cardiolipin-protective compound as a therapeutic agent to restore mitochondrial bioenergetics, Br. J. Pharmacol. 171 (8) (2014) 2029–2050.
[78] C.Y. Kong, et al., Underlying the mechanisms of doxorubicin-induced acute cardiotoxicity: oxidative stress and cell death, Int. J. Biol. Sci. 18 (2) (2022) 760–770.
[79] A. Picca, et al., Mitochondrial quality control mechanisms as molecular targets in cardiac ageing, Nat. Rev. Cardiol. 15 (9) (2018) 543–554.
[80] J.C. Campos, et al., Mitochondrial quality control in cardiac diseases, Front. Physiol. 7 (2016) 479.
[81] Z. Gerhart-Hines, et al., Metabolic control of muscle mitochondrial function and fatty acid oxidation through SIRT1/PGC-1alpha, EMBO J. 26 (7) (2007) 1913–1923.
[82] C.H. Sibylle Jä ger, Julie St-Pierre, Bruce M. Spiegelman, AMP-activated protein kinase (AMPK) action in skeletal muscle via direct phosphorylation of PGC-1_, Proc. Natl. Acad. Sci. USA 104 (29) (2007) 12017–12022.
[83] X. Zhong, E.S.R. de Cassia da Silveira, C. Zhong, Mitochondrial biogenesis in response to chromium (VI) toxicity in human liver cells, Int. J. Mol. Sci. 18 (9) (2017).
[84] Y. Matsushima, Y. Goto, L.S. Kaguni, Mitochondrial Lon protease regulates mitochondrial DNA copy number and transcription by selective degradation of mitochondrial transcription factor A (TFAM), Proc. Natl. Acad. Sci. U. S. A. 107 (43) (2010) 18410–18415.
[85] K. Aquilano, et al., p53 orchestrates the PGC-1alpha-mediated antioxidant response upon mild redox and metabolic imbalance, Antioxidants Redox Signal. 18 (4) (2013) 386–399.
[86] J. Li, et al., p53/PGC-1alpha-mediated mitochondrial dysfunction promotes PC3 prostate cancer cell apoptosis, Mol. Med. Rep. 22 (1) (2020) 155–164.
[87] D.C. Chan, Mitochondria: dynamic organelles in disease, aging, and development, Cell 125 (7) (2006) 1241–1252.
[88] A.H. Chaanine, et al., JNK modulates FOXO3a for the expression of the mitochondrial death and mitophagy marker BNIP3 in pathological hypertrophy and in heart failure, Cell Death Dis. 3 (2) (2012) 265.
[89] M. Ding, et al., Mfn2-mediated mitochondrial fusion alleviates doxorubicin-induced cardiotoxicity with enhancing its anticancer activity through metabolic switch, Redox Biol. 52 (2022) 102311.
[90] S. Gao, J. Hu, Mitochondrial fusion: the machineries In and out, Trends Cell Biol. 31 (1) (2021) 62–74.
[91] R. Liu, D.C. Chan, OPA1 and cardiolipin team up for mitochondrial fusion, Nat. Cell Biol. 19 (7) (2017) 760–762.
[92] A.S. Joshi, et al., Cardiolipin and mitochondrial phosphatidylethanolamine have overlapping functions in mitochondrial fusion in Saccharomyces cerevisiae, J. Biol. Chem. 287 (21) (2012) 17589–17597.
[93] D. Ding, et al., FOXO3a-dependent Parkin regulates the development of gastric cancer by targeting ATP-binding cassette transporter E1, J. Cell. Physiol. 236 (4) (2021) 2740–2755.
[94] M.N. Serasinghe, J.E. Chipuk, Mitochondrial fission in human diseases, Handb. Exp. Pharmacol. 240 (2017) 159–188.
[95] Y. Feng, et al., The machinery of macroautophagy, Cell Res. 24 (1) (2014) 24–41.
[96] S. Liu, et al., Autophagy: regulator of cell death, Cell Death Dis. 14 (10) (2023) 648.
[97] K. Frudd, T. Burgoyne, J.R. Burgoyne, Oxidation of Atg 3 and Atg 7 mediates inhibition of autophagy, Nat. Commun. 9 (1) (2018) 95.
[98] V. Choubey, A. Zeb, A. Kaasik, Molecular mechanisms and regulation of Mammalian mitophagy, Cells 11 (1) (2021).
[99] R. Dhingra, et al., Bnip3 mediates doxorubicin-induced cardiac myocyte necrosis and mortality through changes in mitochondrial signaling, Proc. Natl. Acad. Sci. U. S. A. 111 (51) (2014) E5537–E5544.
[100] N. Koleini, E. Kardami, Autophagy and mitophagy in the context of doxorubicin-induced cardiotoxicity, Oncotarget 8 (28) (2017) 46663–46680.
[101] T. Zhang, et al., BNIP3 protein suppresses PINK1 kinase proteolytic cleavage to promote mitophagy, J. Biol. Chem. 291 (41) (2016) 21616–21629.
[102] D. Faccenda, et al., Control of mitochondrial remodeling by the ATPase inhibitory factor 1 unveils a pro-survival relay via OPA1, Cell Rep. 18 (8) (2017) 1869–1883.
[103] R. Anand, et al., The i-AAA protease YME1L and OMA1 cleave OPA1 to balance mitochondrial fusion and fission, J. Cell Biol. 204 (6) (2014) 919–929.
[104] C. Tung, et al., Elamipretide: a review of its structure, mechanism of action, and therapeutic potential, Int. J. Mol. Sci. 26 (3) (2025).
[105] L.J. Peter, B.M.T.B. de Keizer, Tobias B. Dansen, Forkhead box O as a sensor, mediator, and regulator of redox signaling, Antioxidants Redox Signal. 14 (6) (2011).
[106] G. Cao, et al., The rules and regulatory mechanisms of FOXO3 on inflammation, metabolism, cell death and aging in hosts, Life Sci. 328 (2023) 121877.
[107] D. Davila, et al., Two-step activation of FOXO3 by AMPK generates a coherent feed-forward loop determining excitotoxic cell fate, Cell Death Differ. 19 (10) (2012) 1677–1688.
[108] G. Guan, Y. Chen, Y. Dong, Unraveling the AMPK-SIRT1-FOXO pathway: the In-Depth analysis and breakthrough prospects of oxidative stress-induced diseases, Antioxidants 14 (1) (2025).
[109] A.L. Portbury, et al., Back to your heart: ubiquitin proteasome system-regulated signal transduction, J. Mol. Cell. Cardiol. 52 (3) (2012) 526–537.
[110] S. Clavel, et al., Regulation of the intracellular localization of Foxo3a by stress-activated protein kinase signaling pathways in skeletal muscle cells, Mol. Cell Biol. 30 (2) (2010) 470–480.
[111] B. Sacks, et al., Mitochondrial targeted antioxidants, mitoquinone and SKQ1, not vitamin C, mitigate doxorubicin-induced damage in H9c2 myoblast: pretreatment vs. co-treatment, BMC Pharmacol Toxicol 22 (1) (2021) 49.
[112] B.B. Wu, K.T. Leung, E.N. Poon, Mitochondrial-targeted therapy for doxorubicin-induced cardiotoxicity, Int. J. Mol. Sci. 23 (3) (2022).